Global loss of cellular m 6 A RNA methylation following infection with different SARS-CoV-2 variants

Roshan Vaid, Akram Mendez, Ketan Thombare, Rebeca Burgos-Panadero, Rémy Robinot, Barbara F Fonseca, Nikhil R Gandasi, Johan Ringlander, Mohammad Hassan Baig, Jae-June Dong, et al.

Research

Global loss of cellular m^{6}A RNA methylation following infection with different SARS-CoV-2 variants

Roshan Vaid,[1,9] Akram Mendez,[1,9] Ketan Thombare,[1] Rebeca Burgos-Panadero,[1] Rémy Robinot,[2] Barbara F. Fonseca,[2] Nikhil R. Gandasi,[3] Johan Ringlander,[4] Mohammad Hassan Baig,[5] Jae-June Dong,[5] Jae Yong Cho,[6] Björn Reinius,[7] Lisa A. Chakrabarti,[2] Kristina Nystrom,[4] and Tanmoy Mondal[1,8]

[1]*Department of Laboratory Medicine, Institute of Biomedicine, University of Gothenburg, Gothenburg 41345, Sweden;* [2]*Virus and Immunity Unit, Institut Pasteur, Université Paris Cité, CNRS UMR 3569, Paris, France;* [3]*GA08/NRG-Laboratory, Department of Molecular Reproduction, Development and Genetics, Indian Institute of Sciences, Bengaluru 560012, India;* [4]*Department of Infectious Diseases, Sahlgrenska Academy, University of Gothenburg, Gothenburg 41345, Sweden;* [5]*Department of Family Medicine,* [6]*Department of Internal Medicine, Gangnam Severance Hospital, Yonsei University College of Medicine, Gangnam-gu, Seoul 120-752, Korea;* [7]*Department of Medical Biochemistry and Biophysics, Karolinska Institute, Stockholm 17177, Sweden;* [8]*Department of Clinical Chemistry, Sahlgrenska University Hospital, University of Gothenburg, Gothenburg 41345, Sweden*

Insights into host–virus interactions during SARS-CoV-2 infection are needed to understand COVID-19 pathogenesis and may help to guide the design of novel antiviral therapeutics. N^6-Methyladenosine modification (m^{6}A), one of the most abundant cellular RNA modifications, regulates key processes in RNA metabolism during stress response. Gene expression profiles observed postinfection with different SARS-CoV-2 variants show changes in the expression of genes related to RNA catabolism, including m^{6}A readers and erasers. We found that infection with SARS-CoV-2 variants causes a loss of m^{6}A in cellular RNAs, whereas m^{6}A is detected abundantly in viral RNA. METTL3, the m^{6}A methyltransferase, shows an unusual cytoplasmic localization postinfection. The B.1.351 variant has a less-pronounced effect on METTL3 localization and loss of m^{6}A than did the B.1 and B.1.1.7 variants. We also observed a loss of m^{6}A upon SARS-CoV-2 infection in air/liquid interface cultures of human airway epithelia, confirming that m^{6}A loss is characteristic of SARS-CoV-2-infected cells. Further, transcripts with m^{6}A modification are preferentially down-regulated postinfection. Inhibition of the export protein XPO1 results in the restoration of METTL3 localization, recovery of m^{6}A on cellular RNA, and increased mRNA expression. Stress granule formation, which is compromised by SARS-CoV-2 infection, is restored by XPO1 inhibition and accompanied by a reduced viral infection in vitro. Together, our study elucidates how SARS-CoV-2 inhibits the stress response and perturbs cellular gene expression in an m^{6}A-dependent manner.

[Supplemental material is available for this article.]

The ongoing pandemic of COVID-19 disease is caused by the severe acute respiratory syndrome coronavirus 2 (SARS-CoV-2). Since 2019, the virus has spread over the world, and novel variants have emerged in succession, associated with changes in transmissibility and disease severity capacity (Tao et al. 2021). The SARS-CoV-2 genome consists of a single-stranded positive genomic RNA of approximately 30,000 nucleotides (Wu et al. 2020). Although different vaccines have been developed to mitigate SARS-CoV-2 spreading, it is still necessary to gain knowledge on the basic mechanisms underlying SARS-CoV-2 infection and host response to assist in the development of improved therapeutic options.

N^6-Methyladenosine modification (m^{6}A) is a prevalent internal RNA modification (Baquero-Perez et al. 2021). It is involved in the regulation of a broad range of biological processes including cell differentiation (Geula et al. 2015), mRNA stability, translation, liquid-phase separation, and stress granule formation, among others (Zaccara et al. 2019). The writing of m^{6}A on mRNA is mediated by a methyltransferase complex comprising the core catalytic subunits METTL3 and METTL14 and the adapter subunits WTAP, VIRMA, HAKAI, and RBM15/B (Ping et al. 2014; Patil et al. 2016; Xiao et al. 2016; Yue et al. 2018; Bawankar et al. 2021). The m^{6}A-modified RNAs are recognized by cytoplasmic YTH domain-containing proteins, namely, YTHDF1–YTHDF3, which regulate mRNA stability and stress granule formation. In addition, the nuclear m^{6}A reader proteins YTHDC1 and HNRNPA2B1 play critical roles in splicing and nuclear export (Alarcón et al. 2015; Xiao et al. 2016). Finally, m^{6}A modifications can also be erased by the dioxygenases FTO and ALKBH5, which specifically demethylate m^{6}A RNA (Zhang et al. 2017; Wei et al. 2022).

[9]These authors contributed equally to this work.
Corresponding author: tanmoy.mondal@gu.se
Article published online before print. Article, supplemental material, and publication date are at https://www.genome.org/cgi/doi/10.1101/gr.276407.121. Freely available online through the *Genome Research* Open Access option.

The m^{6}A RNA modification has been identified in several viral genomic RNA, being first described for DNA viruses, such as the simian virus 40 (SV40), herpes simplex virus, and adenovirus 2, and also in retroviruses, such as Rous sarcoma virus and human immunodeficiency virus 1 (HIV-1) (Lu et al. 2018). Moreover, a role for m^{6}A modification has been described for RNA viruses, such as dengue, West Nile fever, yellow fever, Zika, and hepatitis C viruses, in which it was involved in the suppression of viral gene expression and replication (Lichinchi et al. 2016; Kim and Siddiqui 2021). The SARS-CoV-2 genome is m^{6}A-modified by host proteins, and the m^{6}A modification is important for promoting viral replication and for limiting the host immune response (Li et al. 2021; Liu et al. 2021; Zhang et al. 2021b). Depletion of the cytoplasmic m^{6}A readers, the YTHDF proteins, and the writer METTL3 suppress SARS-CoV-2 (and HCoV-OC43) replication. METTL3 inhibition mediated by a small-molecule inhibitor induces viral RNA synthesis suppression, suggesting that m^{6}A modification is needed for optimal viral RNA expression (Burgess et al. 2021).

Though recent studies reported the presence of m^{6}A in the SARS-CoV-2 RNA genome (Kim et al. 2020; Burgess et al. 2021; Li et al. 2021; Liu et al. 2021; Zhang et al. 2021b), it has not been explored in detail how the host's m^{6}A mRNA profile is affected during infection. To address this question, we studied the effect of SARS-CoV-2 infection in Vero cells and air/liquid interface (ALI) cultures of human airway epithelia, which are highly permissive to SARS-CoV-2 infection (Robinot et al. 2021; Wei et al. 2021b).

Results

Infection by different SARS-CoV-2 variants leads to deregulation of RNA catabolism–related genes

To identify variant-specific differences in gene expression perturbations, we infected Vero cells with three SARS-CoV-2 variants: B.1, B.1.1.7, and B.1.351. At 48 h postinfection, spike positivity was detected in 94%–95% of infected cells for all the variants (Supplemental Fig. S1A). We isolated total RNA 48 h postinfection and evaluated gene expression changes using RNA sequencing (RNA-seq). We first checked viral RNA levels postinfection and observed that RNA-seq reads mapping to the viral genome were comparable for the three SARS-CoV-2 variants (Supplemental Fig. S1B). The expression levels analyzed per viral gene were also similar for the three variants (Supplemental Fig. S1C). Viral reads contributed 1.2%–2.8% of the total reads recovered from infected cells (adding reads from the viral and host genomes) (Supplemental Fig. S1D), which is consistent with an earlier report (Blanco-Melo et al. 2020). Next, we performed a differential gene expression analysis to identify genes with altered expression postinfection in Vero cells (Fig. 1A; Supplemental Data S1). We identified a considerable number of up-regulated (998) and down-regulated (950) genes that were modulated across the three variants during infection (Fig. 1B). We then performed a principal component analysis (PCA) and a regression analysis to evaluate similarities in gene expression patterns across the three variants. We observed variant-specific patterns in gene expression, with gene expression patterns being more similar between the B.1.1.7 and B.1.351 variants (Supplemental Fig. S1E,F). Gene expression changes postinfection with three SARS-CoV-2 variants overlapped with several publicly available data sets deposited since the outbreak of COVID-19 (Supplemental Fig. S1G). We also compared the gene expression data set post-SARS-CoV-2 infection in three different variants with one of the publicly available data sets (Riva et al. 2020), in which differential gene expression was analyzed 24 h post-SARS-COV-2 infection in the Vero cells, and we observed a moderate but significant positive correlation between our data and publicly available data (Supplemental Fig. S1H). Pathway analysis revealed that altered genes were enriched in pathways associated with protein localization to the membrane, RNA catabolic processes, and cilium assembly (Fig. 1C; Supplemental Data S2). This was evident in the pathway analysis performed on up- and down-regulated genes separately after viral infection. Up-regulated genes were enriched for pathways related to several RNA catabolic processes, especially in B.1 and B.1.1.7 variants, whereas down-regulated genes were enriched with cilium assembly and organization (Supplemental Fig. S1I; Supplemental Data S2). We then chose to systematically look at the genes involved in RNA catabolic processes that were frequently deregulated across variants during SARS-CoV-2 infection. To do so, we selected RNA catabolism–related pathways, which were enriched in deregulated genes in at least two variants and visualized the interactions of those genes using network analysis (Fig. 1D). We observed that the mean connectivity of nodes in the RNA catabolism pathway–related network was much higher compared with random networks (Supplemental Fig. S1J). In particular, the network analysis suggested widespread interactions (as detected by connectivity degree) of m^{6}A-related genes with different RNA catabolic processes (Supplemental Fig. S1K). We observed that m^{6}A-related genes were frequently deregulated during SARS-CoV-2 infection in Vero cells (Fig. 1E), although we did not observe any significant change in the expression of the main m^{6}A writers *METTL3* and *METTL14*. We validated the differential expression of m^{6}A eraser *FTO*, which was down-regulated, and the up-regulation of the m^{6}A-related genes *SPEN* and *YTHDF1* (Dossin et al. 2020), which was observed after infection with the three variants. Similar changes were observed after infection with the B.1.617.2 (Delta) variant, which was available during the final compilation of the data (Fig. 1F). Although we observed variant-specific gene expression changes, our data suggest widespread deregulation of genes associated with RNA catabolic processes and m^{6}A modification–related pathways for all the SARS-CoV-2 variants tested.

Variant-specific changes in cellular RNA m^{6}A levels after viral infection

A change in m^{6}A-related genes during viral infection prompted us to check the effect of infection on cellular m^{6}A levels. To this end, isolated RNA from noninfected Vero cells and cells infected with three SARS-CoV-2 variants (B.1, B.1.1.7, and B.1.351) was supplemented with spike-in bacterial RNA as a control (spike-in) for m^{6}A RNA immunoprecipitation (RIP) followed by sequencing (m^{6}A RIP-seq) (Fig. 2A). We observed a loss of m^{6}A peaks in the cellular RNA postinfection with different SARS-CoV-2 variants, with the loss of m^{6}A peaks being more marked in the B.1 and B.1.1.7 infections compared with a B.1.351 infection (Supplemental Fig. S2A; Supplemental Data S3). The global distribution of m^{6}A peak density across transcripts in noninfected cells was similar to that reported previously, with strong enrichments near the start and stop codons (Meyer et al. 2012). Spike-in normalized relative m^{6}A peak density showed m^{6}A loss across the whole transcript length following SARS-CoV-2 infection in Vero cells, with more pronounced effects in B.1 and B.1.1.7 infection compared with B.1.351 infection (Fig. 2B). The input RNA signal across the transcript length was largely unaltered between noninfected and different SARS-CoV-2-infected conditions, suggesting input RNA

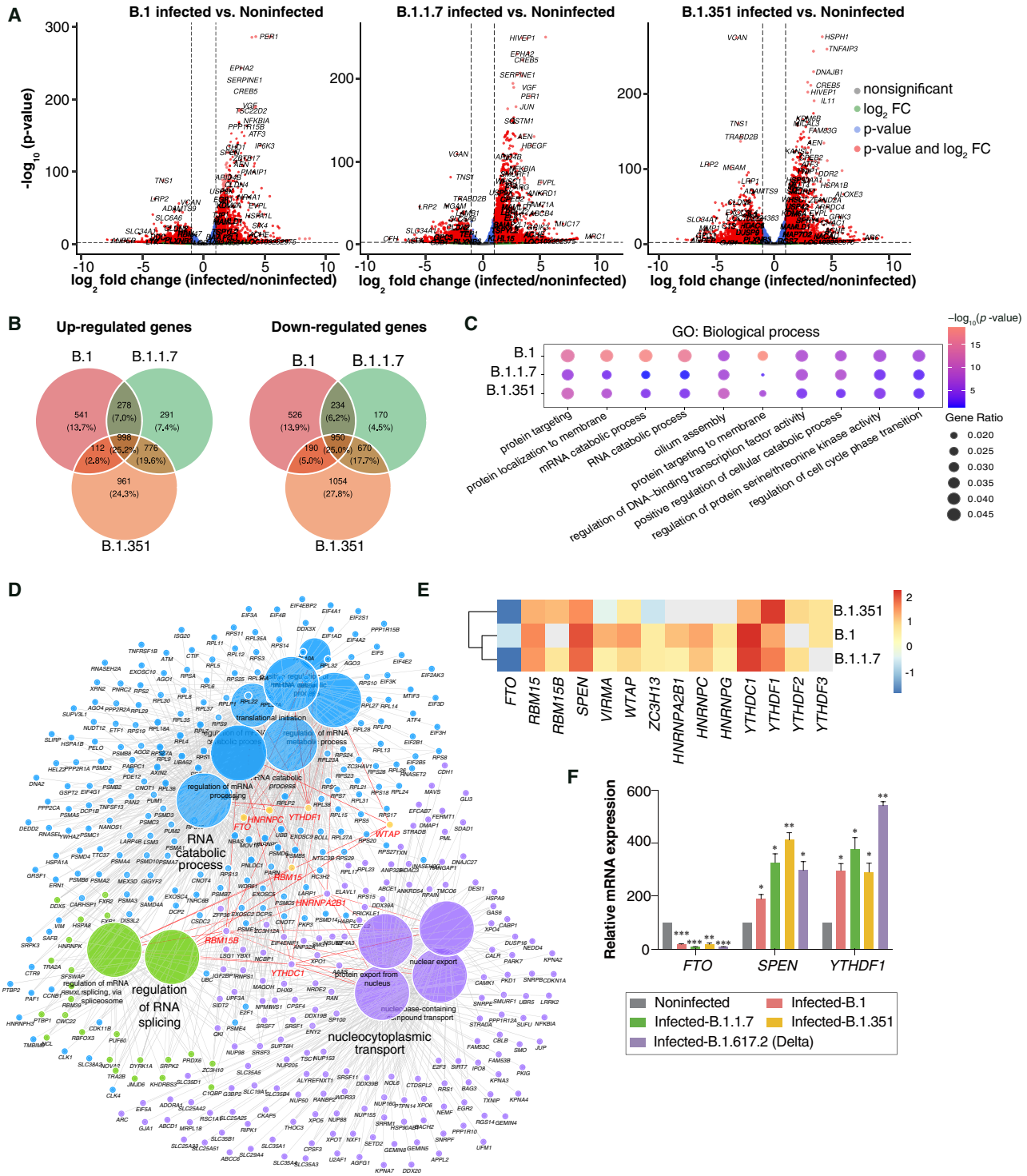

Figure 1. Gene expression changes postinfection with different variants of SARS-CoV-2. (*A*) Volcano plots showing gene expression changes and significance (−log$_{10}$ scale) in SARS-CoV-2-infected versus noninfected cells. Dashed lines indicate the significance threshold (adjusted *P*-value < 0.01) and log$_2$ fold-change threshold (abs log$_2$ fold-change > 1). Differentially expressed genes are highlighted in red, and labels indicate some of the common differentially expressed genes across all conditions. (*B*) Venn diagram comparison of up- and down-regulated genes across variants. (*C*) Top enriched Gene Ontology (GO) term biological processes after infection. The size of the dots represents the enrichment of genes with a GO term, colored according to their significance level. (*D*) ClueGO clustering and visualization of common terms associated with m^{6}A-related genes across any pair of SARS-CoV-2 variants. m^{6}A genes that are deregulated across variants are highlighted in red. (*E*) Heat map of m^{6}A-related genes, with gray boxes indicating nondifferentially expressed genes and colors indicating the log$_2$ fold-change values of significantly deregulated genes in at least two variants. (*F*) Relative mRNA expression of m^{6}A-related genes in noninfected Vero cells and Vero cells infected with B.1, B.1.1.7, B.1.351, and B.1.617.2 (Delta) variants of SARS-CoV-2. *TBP* and *POL2RG* were used to normalize the qPCR data. Data are shown as mean ± SD of three replicates ($n = 3$). Statistics: two-tailed paired *t*-test; (*) $P < 0.05$, (**) $P < 0.01$, (***) $P < 0.001$.

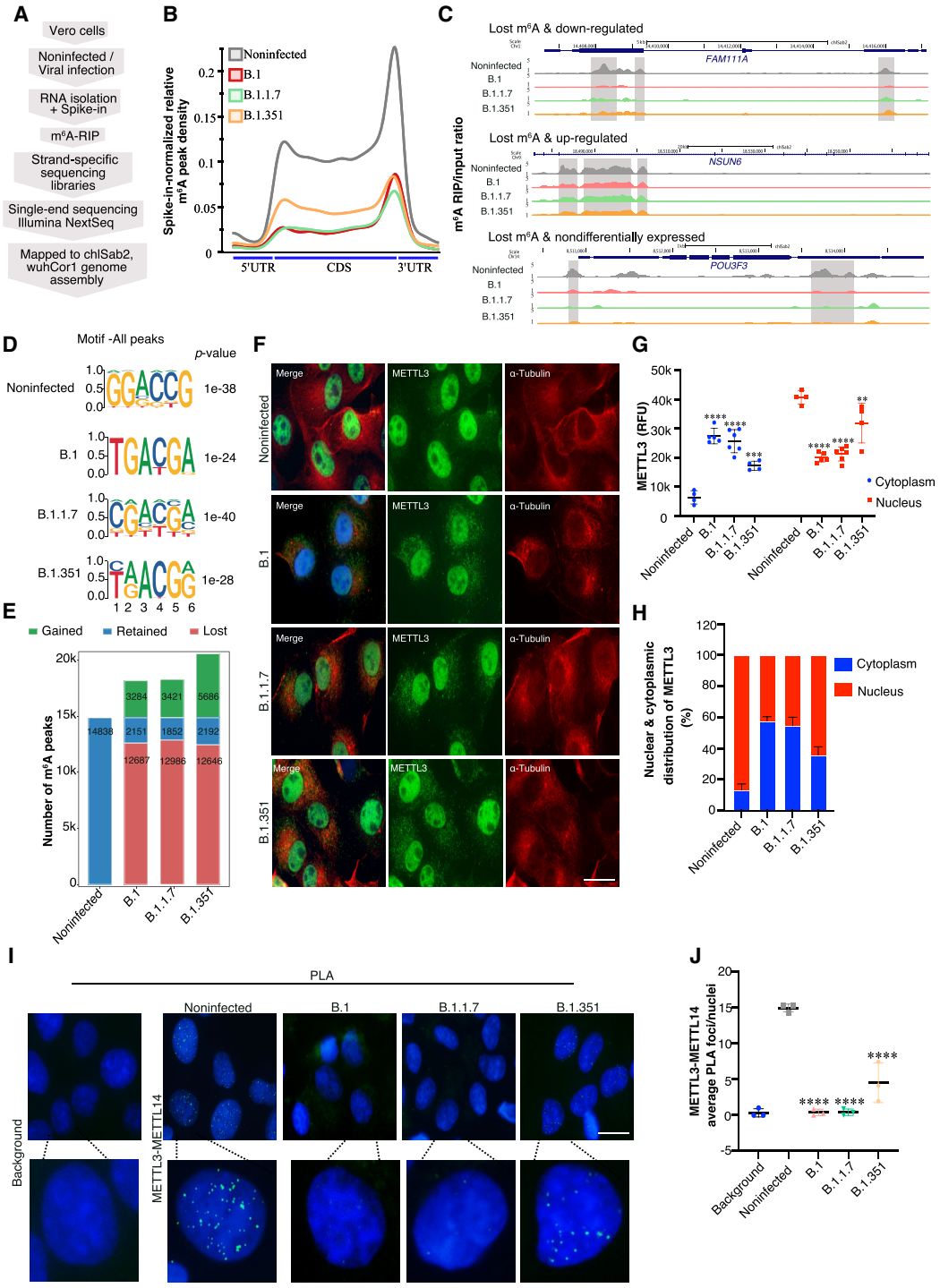

Figure 2. Variant-specific changes in cellular RNA m^{6}A level after viral infection. (*A*) Flow chart describing the m^{6}A RIP-seq protocol. (*B*) Metagene analysis showing spike-in normalized relative m^{6}A peak density at host genes in noninfected and SARS-CoV-2-infected Vero cells (variants as specified by colors). (*C*) Genome browser screenshots showing the ratio of m^{6}A RIP/input for three different genes in noninfected and SARS-CoV-2-infected (variants as specified) Vero cells. Ratio tracks were calculated using spike-in normalized counts per million (CPM). m^{6}A peak regions identified using the MACS peak caller software in noninfected cells are highlighted using gray boxes. (*D*) Identified motifs from de novo motif analysis of peaks in noninfected and infected cells. (*E*) The total number of peaks classified as retained, gained, or lost postinfection with the SARS-CoV-2 variants are indicated and compared with the noninfected condition. (*F–H*) METTL3 localization. (*F*) METTL3 and α-tubulin coimmunostaining in Vero cells that were either noninfected or infected with SARS-CoV-2 variants (as denoted). Scale bar is 20 μm. (*G*) METTL3 intensities (in relative fluorescence units [RFU]) derived from the immunostainings performed in *F*. METTL3 RFU in the nucleus (red) and cytoplasm (blue) were estimated using ImageJ, using DAPI marking the nucleus and α-tubulin staining the cytoplasm as references. Data are shown as mean ± SD. Data presented from multiple experiments with the total number of cells counted, $n = <70$. One-way ANOVA test was performed; (**) $P < 0.01$, (***) $P < 0.001$, (****) $P < 0.0001$. (*H*) Distribution of METTL3 in the nucleus and cytoplasm calculated from the percentage of RFU intensities measured as described in *G*. Data are shown as mean ± SD. (*I,J*) METTL3–METTL14 interaction. (*I*) Proximity ligation assay (PLA) in noninfected and SARS-CoV-2-infected Vero cells (variants as indicated) depicting METTL3 and METTL14 PLA foci in the nucleus (marked by DAPI). The background control shows PLA with only the METTL3 antibody. Scale bar is 20 μm. (*J*) Quantification of METTL3–METTL14 PLA foci as detected in *I*. The number of PLA foci/nuclei are shown as mean ± SD. Data presented from multiple experiments with the total number of cells counted, $n = <100$. One-way ANOVA test was performed; (****) $P < 0.0001$.

does not contribute to the observed m^{6}A loss (Fig. 2B; Supplemental Fig. S2B). This global loss of m^{6}A was also evident by the reduced number of genes with m^{6}A peaks following SARS-CoV-2 infection (Supplemental Fig. S2C). A decrease in the spike-in normalized m^{6}A signal was visible over the commonly lost m^{6}A peaks (Supplemental Fig. S2D) and also at the level of individual transcripts (Fig. 2C) after infection with three SARS-CoV-2 variants. Identified m^{6}A peaks in noninfected cells were enriched with the known "GGAC" motif, whereas the dominant motif was more degenerate in infected cells (Fig. 2D). Although the number of m^{6}A peaks was drastically reduced, we also detected new m^{6}A peaks that were gained over many transcripts after infection with all three variants. The number of gained m^{6}A peaks was highest for the B.1.351 variant (Fig. 2E; Supplemental Fig. S2C). When we investigated the genomic location of the lost and gained peaks during infection, we observed that gained peaks were found in different genomic locations, with major gained peaks located at intergenic and TSS regions (Supplemental Fig. S2F). The most enriched motifs (despite less-significant *P*-values) in the gained m^{6}A peaks were different from the canonical "GGAC" motif (Supplemental Fig. S2E). We also checked by scatter plots the relation between expression ($\log_2$ fold-changes: infected vs. noninfected) and m^{6}A enrichment (infected vs. noninfected) across the transcripts and found that change in expression cannot simply explain alteration in m^{6}A enrichment (Supplemental Fig. S2G). This was further evident in the input RNA signal, which was mostly unaffected over the common lost peaks in infected cells even though the m^{6}A signal was reduced over those peaks (Supplemental Fig. S2D), suggesting the involvement of additional mechanisms that drive m^{6}A loss during SARS-CoV-2 infection.

The global loss of m^{6}A peaks during infection suggests an altered function of the key cellular enzyme complex (METTL3/METTL14), which deposits m^{6}A modifications. The METTL3/METTL14 complex is normally localized in the nucleus and deposits m^{6}A modification cotranscriptionally (Huang et al. 2019). We determined whether METTL3/METTL14 function could be compromised during infection owing to altered cellular localization. We observed that during SARS-CoV-2 infection, METTL3 was partially relocalized from the nucleus to the cytoplasm (Fig. 2F). Importantly, cytoplasmic localization of METTL3 was more evident with the B.1 and B.1.1.7 variants compared with B.1.351 (Fig. 2F–H), which is consistent with a greater reduction in m^{6}A level in B.1 and B.1.1.7 infections. To verify that the METTL3 antibody used was specific and did not detect a viral antigen in infected cells, we infected both control (Control-sh) and *METTL3* knockdown (KD) Vero cells with the B.1 variant (Supplemental Fig. S2H,I). We observed a drastic reduction in METTL3 signal upon *METTL3* KD in noninfected cells. After infection with B.1, the Control-sh cells showed METTL3 localization in both nuclear and cytoplasmic compartments; however, in the *METTL3* KD condition, this staining was absent, suggesting that the METTL3 antibody was indeed specific (Supplemental Fig. S2J). The nuclear localization of METTL14 was mostly unaffected during SARS-CoV-2 infection (Supplemental Fig. S2K). As m^{6}A loss was marked in infected cells, we wondered if partial METTL3 cytoplasmic localization was sufficient to compromise METTL3/METTL14 functional complex formation. To test this, we performed a proximity ligation assay (PLA) to detect the METTL3/METTL14 complex in the noninfected and SARS-CoV-2-infected cells. We observed that the METTL3/METTL14 PLA signal was decreased in infected cells, with an effect that was more marked in B.1 and B.1.1.7 compared with B.1.351, in which METTL3 localization was also less affected (Fig. 2I,J).

SARS-CoV-2 genomic RNA contains m^{6}A modification

Recently several studies reported the presence of m^{6}A modification on SARS-CoV-2 genomic RNA (Burgess et al. 2021; Li et al. 2021; Liu et al. 2021; Zhang et al. 2021b). As we observed that the key m^{6}A depositing enzyme METTL3 showed partial relocalization to the cytoplasm where SARS-CoV-2 genome replication occurs, we investigated the m^{6}A profile in viral RNAs. Our strand-specific m^{6}A RIP sequencing (m^{6}A RIP-seq) data allowed us to profile m^{6}A in both the positive (genomic) and the negative (replicative intermediates) strands of viral RNA for the three SARS-CoV-2 variants. Consistent with previous reports, we detected m^{6}A-enriched regions at several positions of the positive-strand SARS-CoV-2 genome for all three variants, with broader m^{6}A peaks detected in the *N* gene region (Fig. 3A; Supplemental Data S3; Burgess et al. 2021; Li et al. 2021; Liu et al. 2021; Zhang et al. 2021b). Using liquid chromatography–tandem mass spectrometry (LC-MS/MS), we then determined the presence of a relative number of m^{6}A residues in the SARS-CoV-2 RNA genome. In these experiments, viral genomic RNA was isolated from infected Vero cell supernatant, and the ratio of A/m^{6}A was measured using a synthetic m^{6}A-containing RNA oligo as a standard. Using the parallel reaction-monitoring (PRM) mode, we monitored LC-MS/MS profiles for m/z 268.0–136.0 and m/z 282.0–150.1, which correspond to A and m^{6}A, respectively (Sun et al. 2021). We observed that each SARS-CoV-2 genome contains, on average, 10 m^{6}A modifications (Supplemental Fig. S3A), consistent with a recent report (Li et al. 2021). We observed m^{6}A-containing peaks were also present in the negative strand of the viral RNA, mainly in the *N/ORF10* region (Fig. 3B). We then validated the presence of m^{6}A in both the positive and negative strands by strand-specific m^{6}A RIP-qPCR for the B.1.1.7 variant (Fig. 3C). Further, using SARS-CoV-2-infected patient RNA samples from throat/nose swabs, we could detect m^{6}A enrichment in the *N* gene region in both the positive and negative strands of SARS-CoV-2 RNAs (Fig. 3D). We verified up-regulation of selected interferon-stimulated genes in SARS-CoV-2-infected patient throat/nose swab RNA as previously reported (Supplemental Fig. S3B; Gao et al. 2021; Lorè et al. 2021b). The presence of m^{6}A peaks in both strands of SARS-CoV-2 RNA suggests an important functional role for such modifications (Burgess et al. 2021; Li et al. 2021; Liu et al. 2021; Zhang et al. 2021b). Inspection of publicly available viral-RNA protein interaction data shows that m^{6}A reader protein partners are enriched in viral RNA interacting proteins (Schmidt et al. 2021). The m^{6}A readers previously shown to interact with SARS-CoV-2 RNA were searched for known interacting protein partners in the STRING database. We found that these interacting proteins are enriched in RNA metabolism and viral process pathways (Supplemental Fig. S3C, top) and that these proteins show overlap with the SARS-CoV-2 RNA–protein interactome (Supplemental Fig. S3C, bottom). These observations suggest that SARS-CoV-2 may use m^{6}A residues in its genome to recruit other RNA-binding proteins to the viral RNA using m^{6}A readers as intermediates. This is consistent with the recently reported role of m^{6}A reader YTHDF proteins in SARS-CoV-2 infection (Burgess et al. 2021). Given m^{6}A has been implicated in other RNA viruses, the detailed characterization of interactions between m^{6}A readers and SARS-CoV-2 RNA will further elucidate the role of m^{6}A reader proteins in host–virus interactions (Lichinchi et al. 2016; Kim and Siddiqui 2021).

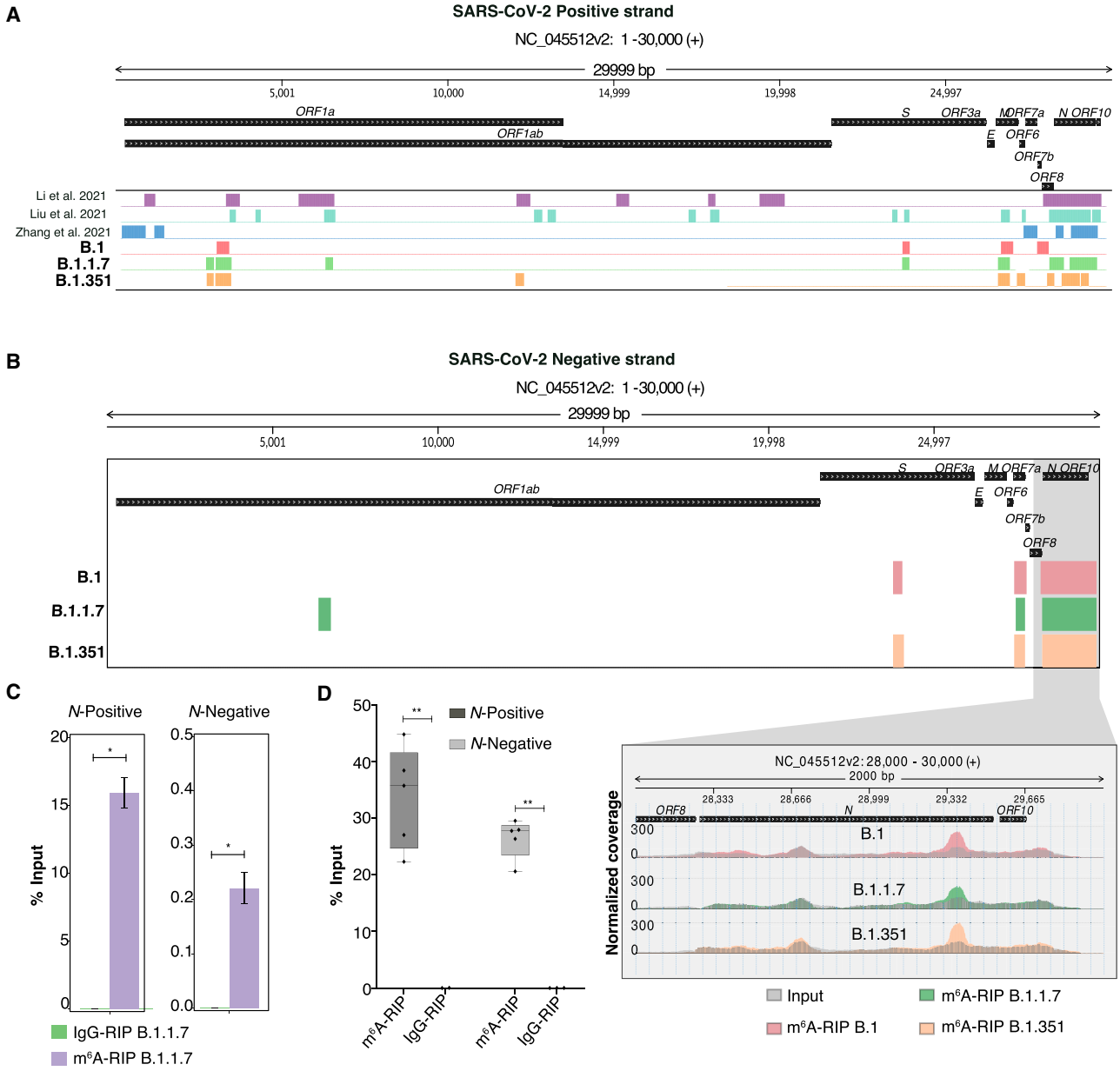

Figure 3. SARS-CoV-2 genomic RNA contains m^{6}A modification. (*A*) Identified m^{6}A peaks on SARS-CoV-2 positive strands from B.1, B.1.1.7, and B.1.351 variants are shown. The m^{6}A peaks in the positive strand of SARS-CoV-2 RNA from publicly available data. (*B*) m^{6}A peaks on the SARS-CoV-2 negative strand. The presence of m^{6}A peaks in the *N* gene region is highlighted, and normalized coverage is shown on the panel *below*. (*C*,*D*) m^{6}A-RIP qPCR data showing enrichment of *N* gene region in both the positive strand and the negative strand of viral RNA. (*C*) Twenty-four hours postinfection with B.1.1.7 in Vero cells; data are represented as a percentage of input, and IgG was used as the negative control. Statistics: two-tailed paired *t*-test, $n = 3$; (*) $P < 0.05$. (*D*) m^{6}A-RIP qPCR data showing enrichment of the *N* gene region in both the positive strand and the negative strand of viral RNA from the infected patient samples ($n = 5$). Data are represented as a percentage of input. IgG was used as a negative control. Statistics: two-tailed paired *t*-test; (**) $P < 0.01$.

m^{6}A loss modulates cellular gene expression in SARS-CoV-2-infected cells

To better understand the effects of m^{6}A modulation on cellular gene expression during viral infection, we first identified the set of transcripts showing a change in m^{6}A level during infection with the three SARS-CoV-2 variants compared with noninfected cells. We then compared the genes with lost m^{6}A (shows loss of at least one m^{6}A peak compared with noninfected cells) or with gained m^{6}A (no m^{6}A peak present in noninfected cells, but one or more m^{6}A peaks gained after infection) with our set of differentially expressed genes (up- and down-regulated during infection). We found that the list of up- and down-regulated genes overlapped with that of genes with lost and gained m^{6}A. In general, down-regulated genes showed higher overlap with lost m^{6}A genes across the three variants, whereas the up-regulated genes were overrepresented in the gained m^{6}A gene category (Fig. 4A). To better understand how loss and gain of m^{6}A contributed to gene expression, we performed a cumulative distribution function (CDF) analysis that measured RNA abundance using RNA-seq data in genes with either

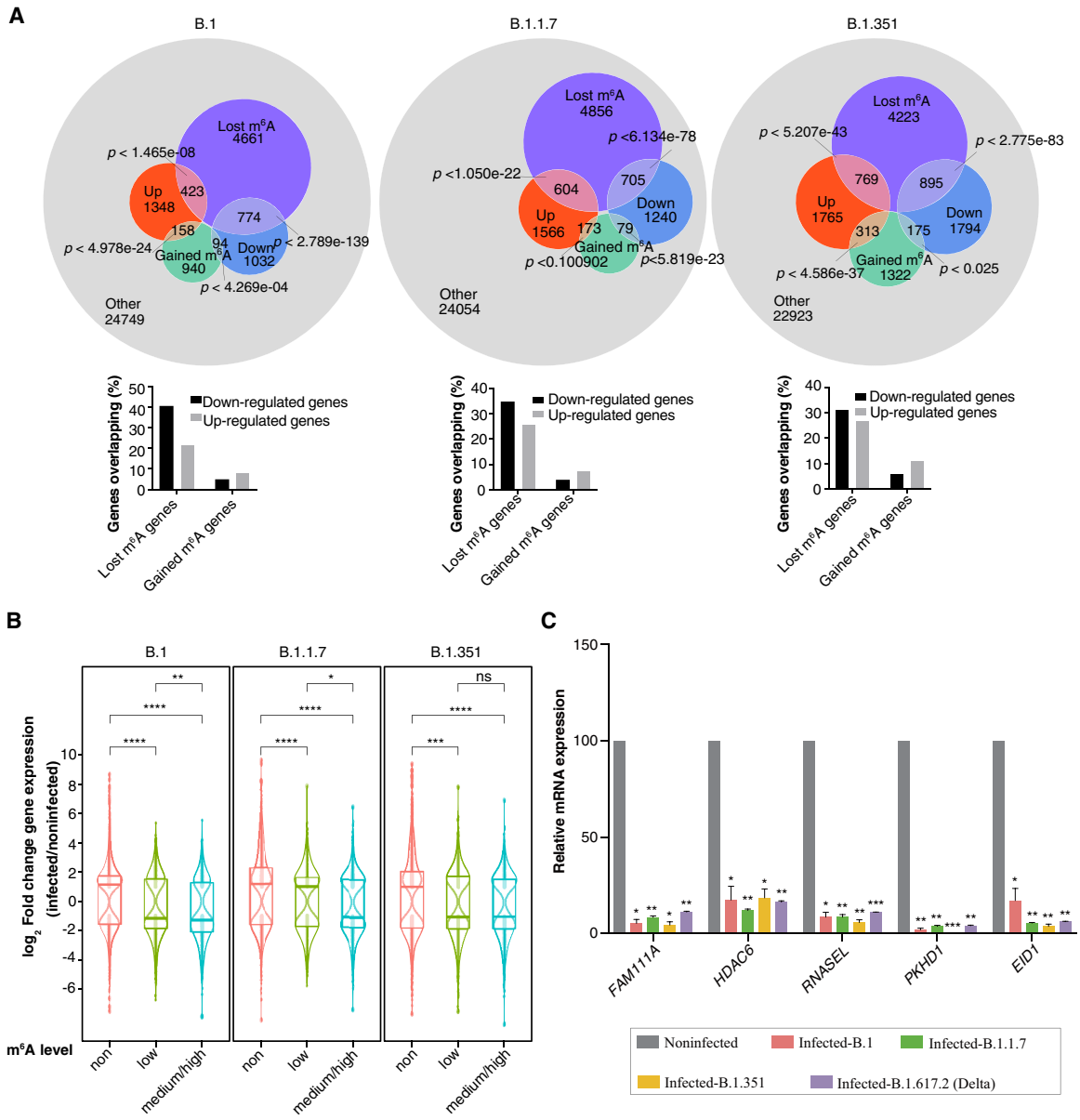

Figure 4. Gene expression after viral infection and global m^{6}A loss. (*A, top*) Overlap diagrams of differentially expressed and m^{6}A-modified genes after infection. Each set shows the number of up-regulated and down-regulated genes associated with lost or gained m^{6}A modifications. The remaining genes are shown in gray. Hypergeometric test *P*-values depict the calculated probability of overlap between differentially expressed and m^{6}A lost/gained genes. (*A, bottom*) Bar-graph summarizing the percentage of up-/down-regulated genes overlapping with either lost or gained m^{6}A genes. (*B*) Log_2 fold-change distributions of differentially expressed genes postinfection with three different variants, categorized according to their m^{6}A level: non, low, medium/high. Statistical significance was calculated using the Wilcoxon test. (ns) Nonsignificant, (*) $P<0.05$, (**) $P<0.01$, (***) $P<0.001$, (****) $P<0.0001$. (*C*) Relative mRNA expression of genes with varying levels of m^{6}A (*FAM111A* and *PKHD1*, high m^{6}A; *HDAC6*, medium m^{6}A; *RNASEL*, low m^{6}A; *EID1*, no m^{6}A) after viral infection with the variant indicated compared with noninfected cells. qPCR data were normalized to *TBP* and *POL2RG*. Statistics: two-tailed *t*-test; (*) $P<0.05$, (**) $P<0.01$, (***) $P<0.001$, $n=2$.

lost or gained m^{6}A peaks. We found that lost m^{6}A genes showed a decrease in abundance, whereas gained m^{6}A genes were increased in abundance after SARS-CoV-2 infection for the three variants studied (Supplemental Fig. S4A). Similar findings were obtained when genes with m^{6}A gain or loss were compared with genes with no change in m^{6}A level (retained genes) (Supplemental Fig. S4B). We further categorized genes in noninfected cells based on m^{6}A content to either non-m^{6}A, low (one peak), medium (two peaks), or high (three or more peaks) m^{6}A. We observed higher-m^{6}A-containing genes were more susceptible to viral infection, with a decreased expression of these genes upon infection with SARS-CoV-2 variants (Fig. 4B). This suggests that m^{6}A modification on these genes contributes to their expression and that their expression is compromised owing to the global loss of m^{6}A during viral infection. We chose a few genes with varying levels of m^{6}A in noninfected cells and validated their down-regulation during viral infection (Fig. 4C). Expression of these genes was also decreased in *METTL3* KD cells, indicating an m^{6}A-dependent expression

(Supplemental Fig. S4C). The exception was *EID1*, which did not change expression in absence of METTL3, consistent with this gene having no m^{6}A modification (Supplemental Fig. S4C). Infection with the B.1.617.2 (Delta) variant also down-regulated the expression of the five tested genes (Fig. 4C). We checked the localization of METTL3 after B1.617.2 infection and observed that METTL3 was partially relocalized from the nucleus to the cytoplasm in B.1.617.2 infection as well (Supplemental Fig. S4D). We then performed a pathway analysis for the up- and down-regulated genes with lost m^{6}A. We observed that down-regulated genes with lost m^{6}A were mostly involved in cilium organization, whereas up-regulated genes with lost m^{6}A were primarily part of pathways related to covalent chromatin/histone modifications (Supplemental Fig. S4E). We validated the down-regulation of some of the known cilia-related genes such as *HDAC6* and *PKHD1* (Fig. 4C; Zhang et al. 2004; Ran et al. 2015) consistent with a recent report suggesting widespread loss of motile cilia after SARS-CoV-2 infection (Robinot et al. 2021). The genes with lost m^{6}A involved in covalent chromatin modification and up-regulated during infection, such as *KDM6A* (Supplemental Data S2), were recently identified as proviral genes in a CRISPR screen (Wei et al. 2021b). Thus, our data suggest that loss of m^{6}A during SARS-CoV-2 infection establishes a pattern of host cell gene expression that favors viral replication.

m^{6}A modification is known to be implicated in alternative splicing (Wei et al. 2021a). Considering the global loss of m^{6}A during SARS-CoV-2 infection, we looked for differential exon use (DEU) in the RNA-seq data. We identified about 790 DEU events common to cells infected with the three SARS-CoV-2 variants (Supplemental Data S4). For instance, we observed that exon 1 of the *COL6A2* collagen gene is differentially included during infection, which is associated with the loss of m^{6}A peaks surrounding the newly included exon 1 (Supplemental Fig. S4F). We also found that DEU-containing genes had on average more m^{6}A peaks compared with random m^{6}A-positive genes in noninfected cells (Supplemental Fig. S4G). Further, we observed that m^{6}A-containing DEU genes showed a loss of m^{6}A peaks during infection (Supplemental Fig. S4H).

Treatment with selinexor restores METTL3 cellular localization during SARS-CoV-2 infection

During the SARS-CoV-2 infection, we observed partial relocalization of METTL3 to the cytoplasm from its original nuclear location. Considering that m^{6}A modification of cellular mRNA is deposited cotranscriptionally in the nucleus (Huang et al. 2019), we aimed to restore METTL3 nuclear localization to see if we could antagonize the effects of SARS-CoV-2 infection. We observed that the expression of *XPO1* (or exportin 1), one of the major nuclear export proteins, was up-regulated during infection (Fig. 5A; Supplemental Fig. S5A). Therefore, we set to determine whether XPO1 was involved in the relocalization of METTL3 during viral infection. Using PLA, we observed that XPO1 and METTL3 interacted with each other in Vero cells (Fig. 5B). We then treated these cells during infection with selinexor, a well-characterized XPO1 inhibitor (Kashyap et al. 2021). We observed that selinexor treatment resulted in the restoration of METTL3 localization to the nucleus of B.1-infected cells (Fig. 5C,D). We then checked if the restoration of METTL3 localization could rescue METTL3/METTL14 complex formation, which was compromised in infected cells. We observed that the METTL3/METTL14 PLA signal was robustly detected in B.1- and B.1.1.7-infected cells treated with selinexor but not in infected cells treated with DMSO (Fig. 5E; Supplemental Fig. S5B). These results suggested that change in METTL3 localization perturbed the formation of the METTL3/METTL14 complex and that promoting METTL3 nuclear localization by selinexor was sufficient to drive the formation of the METTL3/METTL14 complex in infected cells. Importantly, selinexor treatment was also effective in decreasing SARS-CoV-2 infection, as measured by spike protein positivity for all the four variants tested (B.1, B.1.1.7, B.1.351, B.1.617.2), without decreasing cell viability (Supplemental Fig. S5C,D). Of note, the efficacy of selinexor in preventing SARS-CoV-2 infection has also been reported recently (Kashyap et al. 2021).

m^{6}A-modified RNA and m^{6}A reader YTHDF proteins have been implicated in stress granule formation by promoting the recruitment of stress granule proteins such as G3BP1 (Fu and Zhuang 2020). Stress granule formation is known to be compromised in SARS-CoV-2-infected cells, and KD of the stress granule protein G3BP1 enhances SARS-CoV-2 infection (Zheng et al. 2021). We reasoned that the inactivation of stress granule formation by SARS-CoV-2 could be mediated by the global loss of m^{6}A in cellular mRNAs that we uncovered in infected cells. Therefore, we tested if selinexor-mediated reversal of METTL3 nuclear localization could promote stress granule formation in infected cells by reinstalling m^{6}A modification in cellular mRNAs. We observed the appearance of stress granules in selinexor-treated, but not in DMSO-treated (control), SARS-CoV-2-infected cells (Fig. 5F; Supplemental Fig. S5E). Immunostaining showed that stress granules in selinexor-treated infected cells often overlapped with m^{6}A-modified RNAs and with the m^{6}A reader protein YTHDF2 (Fig. 5G; Supplemental Fig. S5F). We then used an RIP assay to check the interaction of four validated mRNAs that show loss of m^{6}A and down-regulation postinfection with the m^{6}A reader YTHDF2 and the stress granule protein G3BP1. Indeed, we found that these mRNAs coprecipitated with both G3BP1 and YTHDF2 (Fig. 5H). Inhibiting the METTL3 enzyme by the small-molecule inhibitor STM2457 (Yankova et al. 2021) decreased the interaction of the four mRNAs with G3BP1 and YTHDF2, suggesting that m^{6}A is required for such interaction (Fig. 5I). METTL3 inhibition did not alter the expression of G3BP1 and YTHDF2 (Supplemental Fig. S5G). Treatment with selinexor, which restored METTL3 nuclear localization during infection, also rescued the expression of the four candidate down-regulated genes, which included the *HDAC6* and *PKHD1* genes related to cilia formation (Fig. 5J). We also observed that selinexor treatment could reinstate the m^{6}A modifications that were lost during infection in these four mRNAs (Fig. 5K). Therefore, rescuing nuclear localization of METTL3 by selinexor promoted stress granule formation in infected cells, restored cellular gene expression, and inhibited SARS-CoV-2 infection in vitro, highlighting the possibility of targeting the m^{6}A pathway as an antiviral strategy.

Global loss of m^{6}A modification in primary human airway epithelial cells upon SARS-CoV-2 infection

Next, we aimed to validate the global loss of m^{6}A methylation during SARS-CoV-2 infection in human cell infection models. To this goal, we tested METTL3 localization post-SARS-CoV-2 infection in the bronchial epithelial cell line, BEAS-2B. BEAS-2B cells were positive for spike protein, and METTL3 showed partial relocalization from the nucleus to the cytoplasm in these infected cells (Fig. 6A; Supplemental Fig. S6A). Further, we also tested METTL3 localization postinfection in primary human bronchial epithelial (HBE) cells grown in monolayer culture, and we observed, similar to

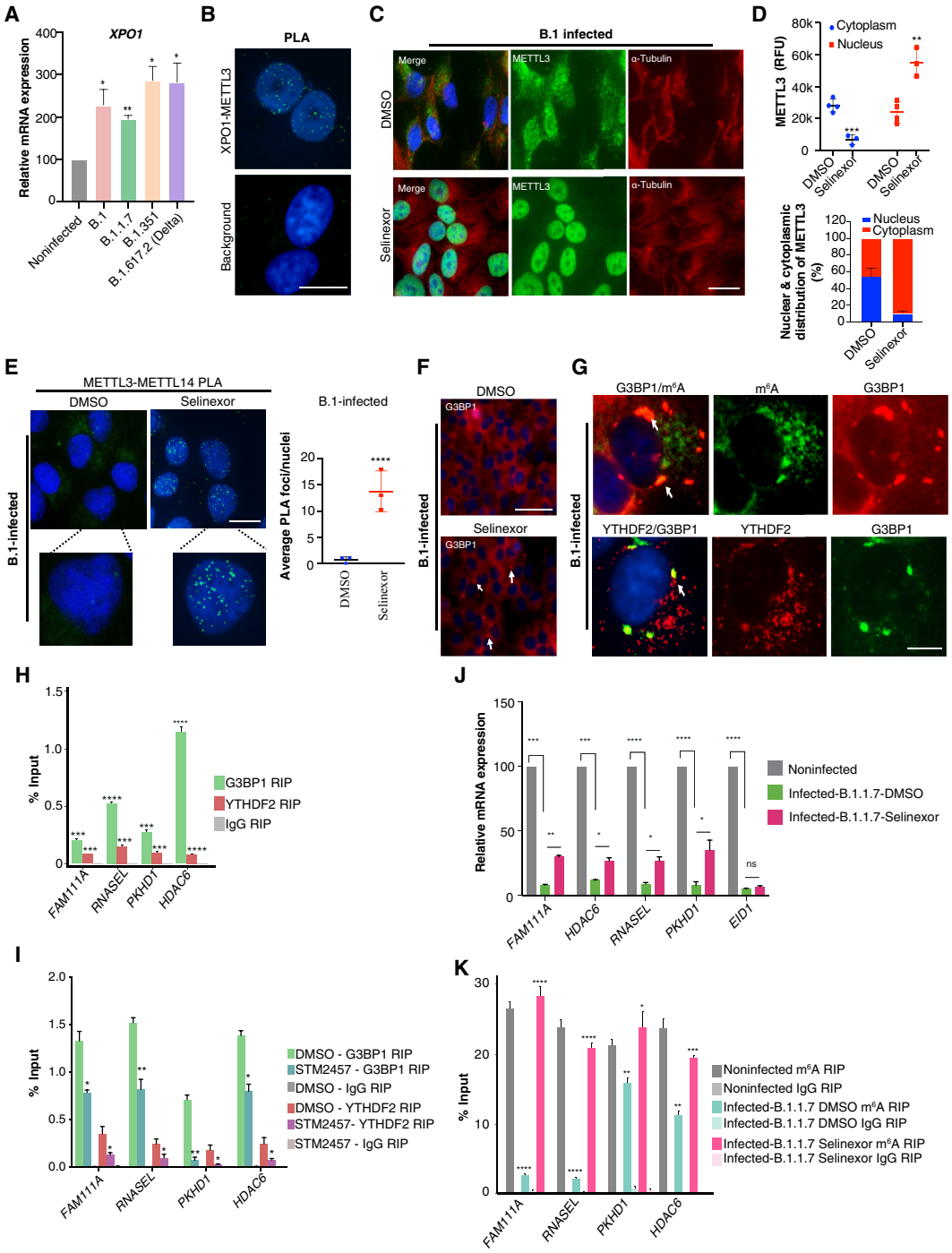

Figure 5. Treatment with selinexor restores METTL3 cellular localization during viral infection. (*A*) Relative expression of the *XPO1* gene evaluated post-SARS-CoV-2 infection (variants as specified) using RT-qPCR. Data were normalized to *TBP* and *POL2RG*. Two-tailed *t*-test; (*) $P<0.05$, (**) $P<0.01$, $n=3$. (*B, top*) PLA in noninfected Vero cells depicting interacting XPO1 and METTL3 foci. (*Bottom*) Background control for PLA with only XPO1 antibody. Scale bar is 20 μm. (*C,D*) Rescue of METTL3 localization. (*C*) METTL3 and α-tubulin coimmunostaining in Vero cells postinfection (24 h) with B.1 SARS-CoV-2 that were either treated with DMSO or selinexor (150 nM). Scale bar is 20 μm. (*D, top*) METTL3 intensities (RFU) from the immunostaining performed in *C*. METTL3 (RFU) in the nucleus and cytoplasm were estimated using ImageJ with help of DAPI marking the nucleus and α-tubulin staining the cytoplasm. Data are shown as Mean ± SD. Data presented from multiple experiments with number of cells counted, $n=<70$. One-way ANOVA test was performed; (**) $P<0.01$, (***) $P<0.001$. (*D, bottom*) Percentage of METTL3 distribution in nucleus and cytoplasm calculated from intensities from the *upper* panel. (*E, top*) PLA depicts interacting METTL3 and METTL14 foci in the nucleus (marked by DAPI) of Vero cells infected with B.1 SARS-CoV-2 variants and treated with either DMSO or selinexor (150 nM). Scale bar is 20 μm. (*E, bottom*) Quantification of METTL3–METTL14 PLA foci as detected in the *above* panel. The number of PLA foci/nuclei are shown as mean ± SD. Data presented from multiple experiments with number of cells counted, $n=>100$. One-way ANOVA test was performed; (****) $P<0.0001$. (*F*) Immunostaining showing G3BP1 localization after DMSO or selinexor (150 nM) treatment in B.1-infected cells (24 h post-infection). White arrow highlights some of the G3BP1 foci. Scale bar is 50 μm. (*G*) Immunostaining showing G3BP1 and m^{6}A/YTHDF2 localization after selinexor treatment in B.1-infected cells (24 h postinfection). White arrow highlights some of the G3BP1 foci overlapping with either m^{6}A or YTHDF2. Scale bar is 10 μm. (*H*) G3BP1 and YTHDF2 RIP showing enrichment of m^{6}A-positive genes in Vero cells. IgG was used as a negative control. Statistics: two-tailed *t*-test; (***) $P<0.001$, (****) $P<0.0001$. $n=4$. (*I*) G3BP1 and YTHDF2 RIP showing enrichment of m^{6}A-positive genes in Vero cells treated with either METTL3 inhibitor STM2457 (5 μM) or DMSO. IgG was used as a negative control. Two-tailed *t*-test; (*) $P<0.05$, (**) $P<0.01$; $n=3$. (*J*) Relative mRNA expression of genes with varying levels of m^{6}A after selinexor treatment in B.1.1.7-infected cells. Treatment with selinexor partially restores the expression of m^{6}A-modified genes (*FAM111A, HDAC6, RNASEL*, and *PKHD1*), but not the non-m^{6}A gene (*EID1*). qPCR data were normalized to *TBP* and *POL2RG*. Statistics: two-tailed *t*-test; (*) $P<0.05$, (**) $P<0.01$, (***) $P<0.001$, (****) $P<0.0001$; $n=3$. (*K*) m^{6}A-RIP qPCR showing recovery of m^{6}A levels at selected genes in selinexor-treated B.1.1.7-infected cells. DMSO was used as treatment control and IgG was used as a negative control for RIP. Two-tailed *t*-test; (*) $P<0.05$, (**) $P<0.01$, (***) $P<0.001$, (****) $P<0.0001$; $n=3$.

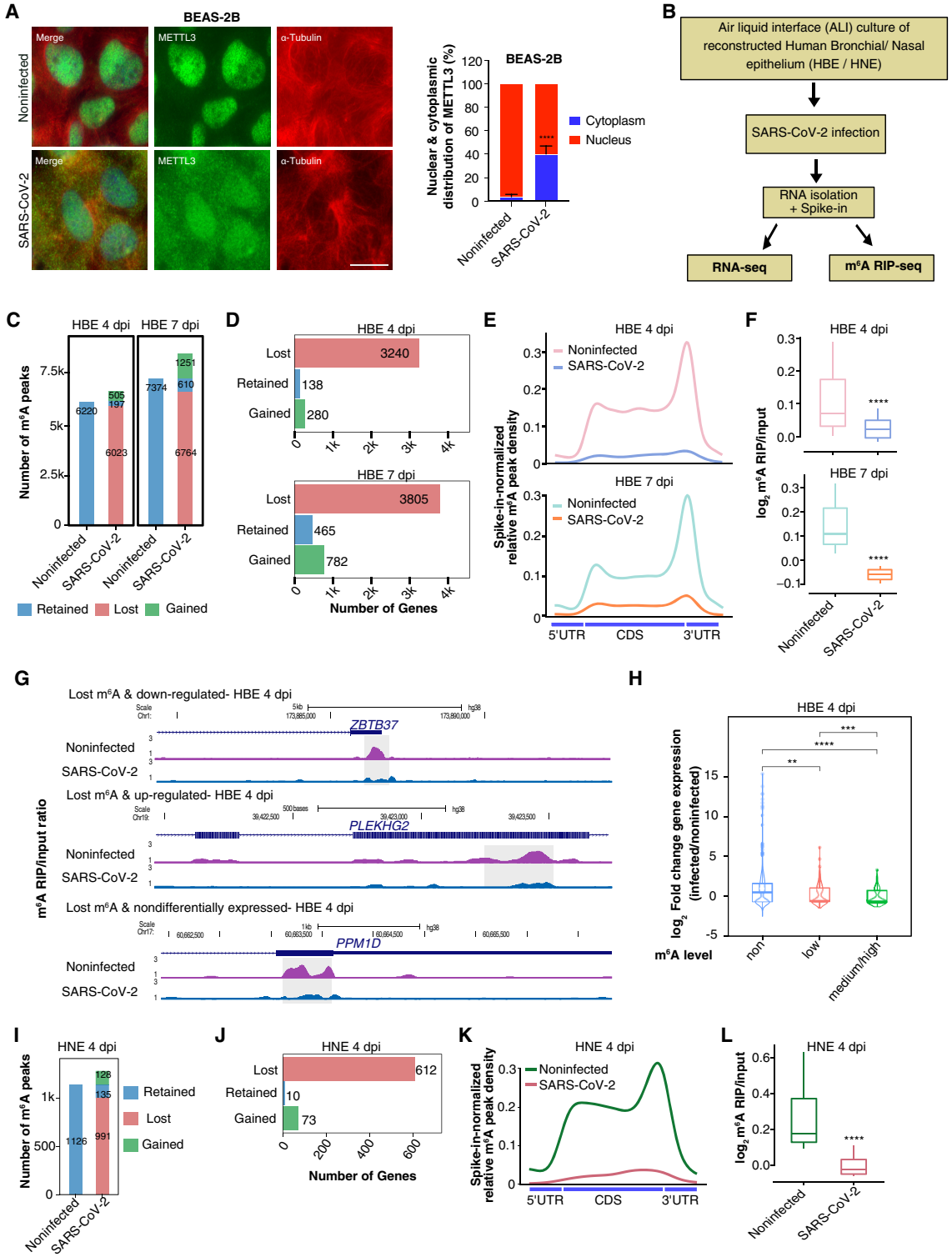

Figure 6. Loss of m^{6}A in human airway epithelia after SARS-CoV-2 infection. (*A*, *left*) METTL3 localization in BEAS-2B cells postinfection with SARS-CoV-2. The scale bar is 20 μm. (*A*, *right*) The percentage distribution of METTL3 in the nucleus and cytoplasm was calculated using ImageJ with help of DAPI marking the nucleus and α-tubulin staining the cytoplasm. Data are shown as mean ± SD. Data presented from multiple experiments with the number of cells counted, $n = <300$. Unpaired *t*-test; (****) $P < 0.0001$. (*B*) Flow chart describing the experimental design for SARS-CoV-2 infection of reconstructed human bronchial/nasal epithelium at ALI. (*C*) Total number of m^{6}A peaks classified as retained, gained, or lost, after 4- or 7-d post infection (dpi) with SARS-CoV-2, compared with noninfected HBE. (*D*) Bar plots representing the number of genes that lost, gained, or retained m^{6}A in HBE after 4 and 7 dpi. (*E*) Metagene plots showing spike-in normalized relative m^{6}A peak density distribution at host genes in noninfected and SARS-CoV-2-infected HBE cells at 4 and 7 dpi. (*F*) Boxplot showing $\log_2$ ratio of m^{6}A signal over input obtained from spike-in normalized CPM data at lost m^{6}A peak regions (±125 bp from m^{6}A peak submit) taken from panel *C* at 4 and 7 dpi in HBE. Statistical significance was calculated using the Wilcoxon test; (****) $P < 0.0001$. (*G*) Genome browser screenshots showing the ratio of m6A RIP/input for three different genes in noninfected and SARS-CoV-2-infected HBE at 4 dpi. Ratio tracks were calculated using spike-in normalized CPM. m^{6}A peak region identified using MACS peak caller in noninfected cells are highlighted using the gray box. (*H*) $\log_2$ fold-change distributions of differentially expressed genes in HBE at 4 dpi, categorized according to their m^{6}A level: non, low, medium/high. Statistical significance was calculated using the Wilcoxon test; (**) $P < 0.01$, (***) $P < 0.001$, (****) $P < 0.0001$. (*I*) Total number of m^{6}A peaks classified as retained, gained, or lost, after 4 dpi with SARS-CoV-2 compared with noninfected HNE. (*J*) The number of genes that lost, gained, or retained m^{6}A in HNE post-SARS-CoV-2 infection. (*K*) Metagene plots showing spike-in normalized relative m^{6}A peak density distribution in noninfected and SARS-CoV-2-infected HNE. (*L*) Boxplot showing $\log_2$ ratio of m^{6}A signal over input obtained from spike-in normalized CPM data at lost m^{6}A peak regions (±125 bp from m^{6}A peak submit) taken from panel *I* at 4 dpi in HNE. Statistical significance was calculated using the Wilcoxon test; (****) $P < 0.0001$.

BEAS-2B, partial cytoplasmic relocalization of METTL3 (Supplemental Fig. S6B,C).

We then used a reconstructed HBE as the SARS-CoV-2 infection model, in which cells are differentiated by the culture at the ALI, forming a pseudostratified ciliated epithelium before viral infection as described previously (Robinot et al. 2021). RNA was extracted from HBE at 4 and 7 days postinfection (dpi), and we observed high levels of SARS-CoV-2 replication as measured by *N* gene expression (Supplemental Fig. S6D). Extracted RNA from HBE at 4 and 7 dpi was supplemented with spike-in bacterial RNA and used in m^{6}A RIP-seq experiments (Fig. 6B). SARS-CoV-2 reads contributed 0.48% and 0.47% of the total reads at 4 and 7 dpi, respectively (Supplemental Fig. S6E). Consistent with our observations in infected Vero cells, we observed a marked loss in the number of m^{6}A peaks postinfection (Fig. 6C; Supplemental Fig. S6F; Supplemental Data S3). The top enriched motif in the m^{6}A peaks from uninfected HBE contained the "GGAC" sequence, whereas the top motif was more degenerate in infected HBE (Supplemental Fig. S6G). A few transcripts showed a gain of m^{6}A during infection in the HBE model, but the fraction of transcripts with gained m^{6}A peaks was much lower compared with that in Vero cells (Fig. 6C). We observed a drastic decrease in the number of m^{6}A-positive genes in HBE on both 4 and 7 dpi (Fig. 6D,E). m^{6}A enrichment (IP/input) and spike-in normalized m^{6}A signal over the lost peaks were significantly reduced in the SARS-CoV-2-infected cells, whereas input RNA was unchanged over these lost peaks (Fig. 6F; Supplemental Fig. S6H). Genome browser visualization of three chosen genes showed the loss of m^{6}A peaks at 4 dpi (Fig. 6G). We could detect m^{6}A peaks in both the positive and negative strands of viral RNA at 4 dpi. We also detected m^{6}A peaks in the positive strand of viral RNA at 7 dpi, but m^{6}A peaks were absent in the negative strand at day 7, possibly because the infection reaches a plateau or has already started to decrease at this stage, as described previously (Supplemental Fig. S6I; Supplemental Data S3; Robinot et al. 2021). Genes related to the defense response to viruses and type I interferon signaling pathways were up-regulated upon SARS-CoV-2 infection in HBE, whereas genes related to cilium organization were the most down-regulated (Supplemental Fig. S6J; Supplemental Data S1,S2). In the HBE infection model, genes containing one or more m^{6}A peaks were prone to down-regulation postinfection, similar to the findings obtained in Vero cells (Fig. 6H). Down-regulated genes with lost m^{6}A were again enriched in the pathways of cilium organization and cilium assembly (Supplemental Fig. S6K), suggesting that m^{6}A loss could be a major contributor to the loss of cilia as previously reported in the HBE model (Robinot et al. 2021). These data collectively confirm that SARS-CoV-2 infection causes a general perturbation of m^{6}A-dependent gene expression in human primary epithelial cells.

We further evaluated changes in cellular m^{6}A level following SARS-CoV-2 infection in reconstructed human nasal epithelia (HNE) cultures in ALI conditions, which also support robust SARS-CoV-2 infection (Fig. 6B; Samelson et al. 2022). We verified SARS-CoV-2 infection in HNE 4 dpi using the expression of the *N* gene (Supplemental Fig. S7A). SARS-CoV-2 reads contributed 0.79% of total reads in the HNE (Supplemental Fig. S7B). Infected HNE showed a drastic loss of m^{6}A peaks 4 dpi and a decrease in the number of m^{6}A-positive genes as well (Fig. 6I–K). As observed in HBE, m^{6}A enrichment (IP/input) and spike-in normalized m^{6}A signal over the lost peaks were significantly reduced in HNE, whereas input RNA was unchanged (Fig 6F; Supplemental Fig. S6H; Fig 6L; Supplemental Fig. S7C). Importantly, infected HNE showed a reduced level of nuclear METTL3 with partial relocalization to the cytoplasm (Supplemental Fig. S7D,E). We observed that infected HNEs were positive for spike protein and showed disturbed staining of cilia marker TUBB4A as reported earlier (Supplemental Fig. S7D; Robinot et al. 2021). Taken together, our observations in multiple transformed and primary cell culture models suggest that SARS-CoV-2 infection causes a global loss of m^{6}A in cellular RNA.

Discussion

We report that SARS-CoV-2 infection causes a global loss of m^{6}A in cellular RNAs while enabling m^{6}A addition in viral RNAs, highlighting how this virus usurps mRNA modification pathways to promote its replication. Mechanistically, we found that SARS-CoV-2 infection induced partial relocalization of the m^{6}A methyltransferase METTL3 from the nucleus to the cytoplasm, which compromised the formation of the METTL3/METTL14 complex in the nucleus and could account for the overall decrease in m^{6}A modification in infected cells. The latter findings are consistent with those of Zhang et al. (2021b), who reported a cytoplasmic localization of both METTL3 and METTL14 along with other m^{6}A reader proteins in SARS-CoV-2-infected Vero cells. The extent of METTL3 cytoplasmic relocalization and its effect on METTL3/METTL14 complex function and m^{6}A levels depended on the viral variants. The B.1 and B.1.1.7 variants induced a more pronounced METTL3 relocalization and a more profound loss of m^{6}A than the B.1.351 variant, suggesting that differences in variant fitness may depend not only on their capacity to escape from the innate and adaptive immune responses (Alefishat et al. 2022) but also on their capacity to perturb gene expression in infected cells. We also observed global loss of m^{6}A peaks in primary human airway epithelial cells during SARS-CoV-2 infection, confirming the generality of our findings. In previous reports, however, a global loss in m^{6}A was not detected in the Huh7 and A459 cell lines following SARS-CoV-2 infection, even though a decrease in m^{6}A peaks was observed near the stop codon region in Huh7-infected cells (Burgess et al. 2021; Liu et al. 2021). The differential effect of SARS-CoV-2 infection on m^{6}A regulation in Huh7 and A549 cells compared with Vero, HBE, and HNE infection models may result from different infection rates and/or different tissue origins of the cell types used (Saccon et al. 2021). Although we observed a global decrease in m^{6}A peaks in infected cells, a fraction of transcripts nevertheless showed a gain in m^{6}A peaks upon infection. These gained m^{6}A modifications may be deposited by residual METTL3/METTL14 in the nucleus or by METTL16, which was recently described to also have m^{6}A writing capacity in mRNAs (Su et al. 2022). Future investigations will be needed to understand how the variant-specific effect on m^{6}A contributes to viral adaptation and how a subset of m^{6}A peaks can be gained during infection.

Gene expression analysis also highlighted common pathways dysregulated by all the SARS-CoV-2 variants tested. We observed in particular that genes associated with RNA catabolism tended to be up-regulated in infected Vero cells. Several genes associated with the m^{6}A pathway, including m^{6}A readers and m^{6}A erasers, were deregulated as well during infection. Change in the RNA splicing pattern of m^{6}A-related genes was recently reported after the acute depletion of METTL3, which was interpreted as a feedback loop to compensate for the acute depletion of m^{6}A (Wei et al. 2021a). In SARS-CoV-2-infected cells, depletion of m^{6}A following METTL3 relocalization and loss of functional METTL3/METTL14 complex in the nucleus probably activates a similar feedback

loop, which could explain why genes involved in RNA catabolism and m^{6}A modification were preferentially deregulated. Our combined analysis of differentially expressed genes and change in m^{6}A peak abundance suggests that, in general, the loss of m^{6}A peaks correlates with decreased RNA expression. However, it is important to consider that loss of m^{6}A was more widespread than mRNA decrease in the infected cells and, thus, that loss of m^{6}A did not always lead to decreased gene expression. Further investigation is needed to decipher the mechanisms that dictate how the loss of m^{6}A influences gene expression during viral infection. Although we have pointed out DEU events in the subset of genes with m^{6}A loss, further study is required to understand the effect of m^{6}A loss on the other cellular genes that show no change in expression. We observed that m^{6}A-containing genes were more prone to down-regulation during infection in both Vero and HBE infection models. The SARS-CoV-2 Nsp1 protein has been shown to inhibit the nuclear export of cellular RNAs during infection and to promote host mRNA decay (Burke et al. 2021; Zhang et al. 2021a). The nuclear export of cellular RNA is known to be regulated by m^{6}A in a YTHDC1-dependent and nuclear transcription factor, X-box binding 1 (NFX1)–dependent manner (Roundtree et al. 2017). Viral protein Nsp1 also inhibits NFX1 function, resulting in the retention of cellular mRNAs in the nucleus during SARS-CoV-2 infection (Zhang et al. 2021a). It will be interesting to determine if the loss of m^{6}A and Nsp1-mediated inhibition of NFX1 act synergistically to cause nuclear retention of cellular mRNAs during infection and if the retained mRNAs might be prone to degradation.

Using a strand-specific m^{6}A RIP-seq approach, we found that both the viral genomic RNA (positive-strand) and replicative negative-strand RNAs carried m^{6}A modification. In the HBE model, we detected a robust m^{6}A peak signal in genomic RNA at 4 and 7 dpi. The m^{6}A peaks were also present in the replicative negative strand at 4 dpi, but not at day 7, presumably because viral replication had already abated at this time point. In a previous report by Liu et al. (2021), m^{6}A peaks could be detected on negative-strand of SARS-CoV-2 using m^{6}A RIP-seq, but not with the m^{6}A cross-linking and immunoprecipitation (CLIP) technique. The investigators suggested lack of m^{6}A detection could be owing to the limited coverage of the negative strand in CLIP data (Liu et al. 2021). Although our data from Vero and HBE infection models suggest the presence of m^{6}A peaks in the negative strand, future experiments using m^{6}A-CLIP in the human cell infection model will be required to precisely identify the specific residues modified by m^{6}A. Viral RNA m^{6}A modification is known to have a proviral effect by allowing escape from RIG-I binding and limiting the induction of inflammatory gene expression (Li et al. 2021). As RIG-I is known to be activated by viral double-stranded replicative intermediates (Yamada et al. 2021), it will be interesting to check if the m^{6}A modifications detected in the replicative negative strand of SARS-CoV-2 contribute to an escape mechanism from RIG-I. Although the majority of m^{6}A peaks were similar across the three SARS-CoV-2 variants studied, there were m^{6}A peaks that were specific to particular variants. Further detailed studies will be required to understand if the differences in m^{6}A modification across variants contribute to changes in pathogenicity by differential recruitment of m^{6}A reader proteins or by modulating the RIG-I-dependent escape mechanisms described above.

To explore new therapeutic options against SARS-CoV-2 infection, we have exploited the altered localization of the m^{6}A writer METTL3. We succeeded in restoring METTL3 localization during infection by inhibiting XPO1 with selinexor. Selinexor treatment also increased the expression of specific genes that showed down-regulation with concomitant loss of m^{6}A during infection. XPO1 inhibition by selinexor was previously proposed to be effective in limiting SARS-CoV-2 infection by promoting the nuclear relocalization of the ACE2 receptor (Kashyap et al. 2021). Our study provides a further mechanistic explanation for the effectiveness of XPO1 inhibition during SARS-CoV-2 infection. Although we provide evidence that altered METTL3 localization could be mediated by XPO1, we do not rule out other possible mechanisms that might affect METTL3 localization during SARS-CoV-2 infection. In particular, cytokines that are secreted by infected cells might influence METTL3 localization in both infected and bystander cells, resulting in broad perturbations in cellular m^{6}A, a notion that requires further investigation. Cellular m^{6}A-modified RNAs and m^{6}A reader YTHDF proteins promote stress granule formation, which contributes to the antiviral defense (Fu and Zhuang 2020). The SARS-CoV-2 N-protein has been shown to phase-separate with the stress granule protein G3BP1 and thereby prevent stress granule formation in the infected cells (Wang et al. 2021). We propose an additional mechanism for the inhibition of stress granule formation through the depletion of m^{6}A on cellular RNA. The recovery of stress granules formation in selinexor-treated infected cells may indeed result from restored m^{6}A levels in cellular RNA, which could be visualized by the colocalization of G3BP1, m^{6}A, and YTHDF2. We observed that selinexor treatment also had functional consequences, by restoring the gene expression and m^{6}A enrichment during infection. The recovery of stress granules may have also contributed to stabilizing these RNAs, as association with stress granule proteins such as G3BP1 has been shown to regulate the stability of cellular RNAs (Laver et al. 2020; Somasekharan et al. 2020). Some of the validated m^{6}A-dependent RNAs showed an association with G3BP1 and YTHDF2, suggesting that these RNAs could indeed be guided to stress granules in an m^{6}A-dependent manner.

Collectively, our findings highlight how SARS-CoV-2 perturbs the m^{6}A RNA modification pathway to deregulate cellular RNAs and limit stress granule formation. Change in the cellular localization of METTL3 in infected cells resulted in a global loss of m^{6}A in cellular mRNAs, whereas viral RNAs remained m^{6}A modified. We propose that rescuing METTL3 localization during infection could be explored as a novel antiviral strategy against SARS-CoV-2.

Methods

Cell culture, SARS-CoV-2 infection, and XPOI inhibitor treatment

SARS-CoV-2 was isolated from samples with viral genomes sequenced at the diagnostic laboratory (Ringlander et al. 2021). Isolates from the B.1, B.1.1.7, B.1.351, and B.1.617.2 pango lineages were used to infect Vero CCL-81 cells (ATCC) grown in DMEM, 1% penicillin–streptomycin, and 2% fetal calf serum at 37°C and in 5% CO_2. Details of the infection method in Vero cells, primary HBE cells (Lonza CC-2540S), and bronchial epithelial cell line BEAS-2B (ATCC) and XPO1 treatment are described in the Supplemental Material. SARS-CoV-2 infection of reconstructed human bronchial and nasal epithelia is also described in the Supplemental Material.

Immunofluorescence staining

Immunofluorescence staining was performed in Vero cells, primary HBE cells, and bronchial epithelial cell line BEAS-2B cells using the method as described in the Supplemental Material.

HNE MucilAir cultures were fixed and cut using a scalpel blade, and immunofluorescence staining was performed as described in the Supplemental Material.

RNA-seq and m^{6}A RIP-seq

RNA was isolated from both SARS-CoV-2-infected (48 h postinfection) and noninfected (mock) Vero cells using TRIzol reagent (Thermo Fisher Scientific 15596026) and direct-zol RNA miniprep (ZYMO Research R2050). For RNA extraction of primary epithelial cultures, cells were washed in cold PBS and then lyzed in 150 µL of TRIzol reagent (Thermo Fisher Scientific) added to the apical side of the insert. RNA was purified using the direct-zol miniprep kit (Zymo Research ZR2080), according to the manufacturer's specifications. HBE RNA was isolated at 4 and 7 dpi, whereas HNE RNA was isolated at 4 dpi along with the corresponding noninfected controls.

RNA isolated either from Vero cells (15 µg) or from epithelial culture (5 µg) was supplemented with 10 ng or 3 ng of bacterial RNA, respectively, as a spike-in control, before fragmentation using RNA fragmentation reagents (Thermo Fisher Scientific AM8740). The fragmented RNA was used in RNA-seq and m^{6}A RIP-seq experiments.

Sequencing libraries for total RNA-seq/input for m^{6}A RIP-seq were prepared from 10 ng of the fragmented RNA using SMARTer stranded total RNA-seq kit V2, pico input mammalian (Takara Bio). m^{6}A RIP was performed with fragmented RNA as previously described (Zeng et al. 2018) with m^{6}A antibody (Synaptic Systems 202003) incubated with 15 µg of Vero or 5 µg of epithelial (HBE and HNE) RNA. m^{6}A RIP RNA was used to make sequencing libraries using the SMARTer stranded total RNA-seq kit V2, pico input mammalian (Takara Bio). All the libraries were single-end sequenced (1× 88 bp) on an Illumina NextSeq 2000 platform at the BEA core facility, Stockholm, Sweden.

RT-qPCR and m^{6}A RIP-qPCR

The method followed for RT-qPCR and m^{6}A RIP-qPCR are described in the Supplemental Material, and the primers used in this study are listed in Supplemental Table S1.

Processing of RNA-seq data

Single-end sequencing reads from SMARTer stranded total RNA-seq kit v2 were analyzed with FastQC for quality control (https://www.bioinformatics.babraham.ac.uk/projects/fastqc/), and adapters were removed using Trim Galore! v0.6.6 (https://github.com/FelixKrueger/TrimGalore) with a minimal length threshold of 20 bp. Trimmed reads from Vero infected and noninfected cells were aligned to the following reference genomes: concatenated chlSab2 (*Chlorosebus sabeus*), wuhCor1 (SARS-CoV-2), plus *Escherichia coli* str. K-12 substr. MG1655 (spike-in), or the SARS-CoV-2 + *E. coli* genomes, obtained from the UCSC Genome Browser (http://hgdownload.soe.ucsc.edu/goldenPath/). Alignments were made using HISAT2 v2.2.1 (Kim et al. 2019) with the parameters (-U --rna-strandness R). Sequencing data from human bronchial and nasal epithelial noninfected and infected cells were mapped to the concatenated human (hg38) + SARS-CoV-2 (wuhCor1) + *E. coli* (spike-in) reference genomes. Duplicate alignments were labeled using MarkDuplicates from Picard v2.23.4 (http://broadinstitute.github.io/picard), and marked alignment files were further processed using Sambamba v0.7.1 (Tarasov et al. 2015; Kim et al. 2019), keeping only mapping reads separated by strand after duplicate removal.

Analysis of RNA-seq data for differential gene expression

Differential gene expression following SARS-CoV-2 infection and Gene Ontology (GO) analysis is described in detail in the Supplemental Material.

m^{6}A RIP-seq data analysis

m^{6}A peak calling on SARS-CoV-2 viral genome and infected cell samples was performed with callpeak from MACS2 v2.2.6 (Zhang et al. 2008) on IP and input processed alignments mapped to SARS-CoV-2 wuhCor1 or the concatenated genomes (chlSab2 + wuhCor1) or (hg38 + wuCor1), using the parameters "--no-model --keep-dup auto --call-summits" and effective genome sizes according to each genome with a *P*-value cutoff of 0.05 for SARS-CoV-2 genome and a *P*-value cutoff of 0.01 for the Vero and human data sets. Samples processed using MACS2 were scaled by default to the library size to account for differences during peak calling.

The called peaks were annotated according to the nearest genomic feature using annotatePeaks.pl from HOMER v4.11 (Heinz et al. 2010). Retained, gained, and lost peaks between noninfected and infected cells were identified using BEDTools intersect from BEDTools v2.29.2 (Quinlan and Hall 2010). Briefly, peaks were classified as "retained" depending on whether a peak was intersected between noninfected and infected samples; "lost" if a peak was present in noninfected cells but not intersecting with peaks of infected samples; and "gained" if a peak was present in infected cells but not in noninfected cells. Motif analysis on m^{6}A called peaks was performed with findMotifsGenome.pl from HOMER and visualized with the universalmotif R package (https://bioconductor.org/packages/universalmotif/) using R computing language (R core team 2022). Changes in overall m^{6}A enrichment across transcripts after infection were calculated by extracting the spike-in normalized m^{6}A/input signals from bigWig files within the annotated gene coordinates in the chlsab2 genomes using the rtracklayer package (Lawrence et al. 2009). Further correlation between m^{6}A enrichment and gene expression changes ($\log_2$ fold-changes infected vs. noninfected) were then generated. Potential *N*6,2′-*O*-dimethyladenosine (m6Am) signals were removed from m^{6}A RIP-seq data using the method as described in the Supplemental Material.

Normalization of m^{6}A RIP-seq data using spike-ins

To control for systematic variations across m^{6}A RIP experiments, the amount of spike-in bacterial RNA was estimated by counting the total number of reads uniquely mapped to the *E. coli* K-12 reference genome using Sambamba v0.7.1 (Tarasov et al. 2015). *E. coli* spike-in counts were further used to calculate scaling factors for each batch of m^{6}A RIP-seq samples (Supplemental Table S2). Computed scaling factors were then used in metagene density distribution analyses (described below) to normalize the density of m^{6}A peaks to the spike-in content in each sample. Genome-wide coverage tracks were calculated using normalized counts per million (CPM) and further adjusted according to the computed spike-in scaling factors for m^{6}A and input RNA signals using the bamCoverage –scaleFactor parameter from deepTools v3.3.2 (Ramírez et al. 2016). m^{6}A RIP/input ratio tracks were then calculated using the bigwigCompare function from deepTools.

Metagene analysis

To analyze the genome-wide distribution of m^{6}A, a metagene analysis of m^{6}A peak density distribution was performed by overlapping the peak coordinates with the following genomic features: 5′ UTR, CDS, and 3′ UTR obtained from the GTF genome

annotation files from UCSC (for chlsab2) or GENCODE v36 (for hg38), considering the longest isoform for each gene. Each transcript was scaled to fixed-size metagene bins according to each reference genome. m^{6}A peak density distribution profiles were generated after mapping the m^{6}A peaks to the metagene coordinates using the plyranges R package (Lee et al. 2019). To compare multiple conditions, the relative m^{6}A density distributions were calculated using the relative density function from the ggmulti package (https://cran.r-project.org/web/packages/ggmulti/index.html). The relative density function calculates the sum of the density estimate area of all conditions, where the total sum is scaled to a maximum of one and the area of each condition is proportional to its own count. The relative m^{6}A-RIP peak distributions were further normalized using the calculated spike-in factors.

Enrichment of m^{6}A peaks

To calculate the enrichment of RIP signals across m^{6}A peak regions, we extracted the number of reads in m^{6}A-RIP (m^{6}A signal) and input RNA alignments 125 bp around peak summit coordinates using the ScoreMatrix function from the genomation package using the parameter rpm = TRUE to obtain normalized CPM counts to account for differences of library sizes (Akalin et al. 2015). The m^{6}A-RIP and input RNA signals around 125-bp peak summits were further normalized using spike-in factors. The $\log_2$ ratio of m^{6}A signal/input RNA was then calculated using the enrichmentMatrix function from the same package.

Data access

All raw and processed sequencing data generated in this study have been submitted to the NCBI Gene Expression Omnibus (GEO; https://www.ncbi.nlm.nih.gov/geo/) under accession number GSE188477. The source code used for the analysis of data in this study is available at GitHub (https://github.com/AkramMendez/m6a_sarscov2) and as Supplemental Code.

Competing interest statement

The authors declare no competing interests.

Acknowledgments

We thank the core facility at Novum, BEA, Bioinformatics and Expression Analysis, which is supported by the board of research at the Karolinska Institute and the research committee at the Karolinska hospital for help with sequencing, and the Proteomic core facility at GU for their support with LC-MS/MS. The computations and data handling were enabled by resources in project SNIC-2022-22-85 provided by the Swedish National Infrastructure for Computing (SNIC) at UPPMAX, partially funded by the Swedish Council through grant agreement no. 2018-05973. We acknowledge Anders Sjölander for assistance concerning technical and implementational aspects of the UPPMAX resources. This work was funded by grants from the Swedish Research Council (Vetenskapsrådet) to T.M. (2018-02224), Sweden-South Korea COVID-19 grant from the Swedish Research Council (Vetenskapsrådet) to T.M. (2020-06311 and 2022-05965), and project grant to T.M. from Svenska Läkaresällskapet; Kungl. Vetenskaps- och Vitterhets-Samhället (KVVS) grant to T.M.; grants COROCHIP and PFR7 from the Urgence COVID-19 Fundraising Campaign of Institut Pasteur to L.A.C.; Bollan scholarship to R.V.; and grants from the National Research Foundation of Korea to J.-J.D. (NRF-2021K1A4A7A02098793) and J.Y.C. (NRF-2022K1A3A1A47088296).

References

Akalin A, Franke V, Vlahoviček K, Mason CE, Schübeler D. 2015. genomation: a toolkit to summarize, annotate and visualize genomic intervals. *Bioinformatics* **31:** 1127–1129. doi:10.1093/bioinformatics/btu775

Alarcón CR, Goodarzi H, Lee H, Liu X, Tavazoie S, Tavazoie SF. 2015. HNRNPA2B1 is a mediator of m^{6}A-dependent nuclear RNA processing events. *Cell* **162:** 1299–1308. doi:10.1016/j.cell.2015.08.011

Alefishat E, Jelinek HF, Mousa M, Tay GK, Alsafar HS. 2022. Immune response to SARS-CoV-2 variants: a focus on severity, susceptibility, and preexisting immunity. *J Infect Public Health* **15:** 277–288. doi:10.1016/j.jiph.2022.01.007

Baquero-Perez B, Geers D, Díez J. 2021. From A to m^{6}A: the emerging viral epitranscriptome. *Viruses* **13:** 1049. doi:10.3390/v13061049

Bawankar P, Lence T, Paolantoni C, Haussmann IU, Kazlauskiene M, Jacob D, Heidelberger JB, Richter FM, Nallasivan MP, Morin V, et al. 2021. Hakai is required for stabilization of core components of the m^{6}A mRNA methylation machinery. *Nat Commun* **12:** 3778. doi:10.1038/s41467-021-23892-5

Blanco-Melo D, Nilsson-Payant BE, Liu W-C, Uhl S, Hoagland D, Møller R, Jordan TX, Oishi K, Panis M, Sachs D, et al. 2020. Imbalanced host response to SARS-CoV-2 drives development of COVID-19. *Cell* **181:** 1036–1045.e9. doi:10.1016/j.cell.2020.04.026

Burgess HM, Depledge DP, Thompson L, Srinivas KP, Grande RC, Vink EI, Abebe JS, Blackaby Wesley P, Hendrick A, Albertella MR, et al. 2021. Targeting the m^{6}A RNA modification pathway blocks SARS-CoV-2 and HCoV-OC43 replication. *Genes Dev* **35:** 1005–1019. doi:10.1101/gad.348320.121

Burke JM, St Clair LA, Perera R, Parker R. 2021. SARS-CoV-2 infection triggers widespread host mRNA decay leading to an mRNA export block. *RNA* **27:** 1318–1329. doi:10.1261/rna.078923.121

Dossin F, Pinheiro I, Żylicz JJ, Roensch J, Collombet S, Le Saux A, Chelmicki T, Attia M, Kapoor V, Zhan Y, et al. 2020. SPEN integrates transcriptional and epigenetic control of X-inactivation. *Nature* **578:** 455–460. doi:10.1038/s41586-020-1974-9

Fu Y, Zhuang X. 2020. m^{6}A-binding YTHDF proteins promote stress granule formation. *Nat Chem Biol* **16:** 955–963. doi:10.1038/s41589-020-0524-y

Gao X, Liu Y, Zou S, Liu P, Zhao J, Yang C, Liang M, Yang J. 2021. Genome-wide screening of SARS-CoV-2 infection-related genes based on the blood leukocytes sequencing data set of patients with COVID-19. *J Med Virol* **93:** 5544–5554. doi:10.1002/jmv.27093

Geula S, Moshitch-Moshkovitz S, Dominissini D, Mansour AA, Kol N, Salmon-Divon M, Hershkovitz V, Peer E, Mor N, Manor YS, et al. 2015. Stem cells. m^{6}A mRNA methylation facilitates resolution of naïve pluripotency toward differentiation. *Science* **347:** 1002–1006. doi:10.1126/science.1261417

Heinz S, Benner C, Spann N, Bertolino E, Lin YC, Laslo P, Cheng JX, Murre C, Singh H, Glass CK. 2010. Simple combinations of lineage-determining transcription factors prime *cis*-regulatory elements required for macrophage and B cell identities. *Mol Cell* **38:** 576–589. doi:10.1016/j.molcel.2010.05.004

Huang H, Weng H, Zhou K, Wu T, Zhao BS, Sun M, Chen Z, Deng X, Xiao G, Auer F, et al. 2019. Histone H3 trimethylation at lysine 36 guides m^{6}A RNA modification co-transcriptionally. *Nature* **567:** 414–419. doi:10.1038/s41586-019-1016-7

Kashyap T, Murray J, Walker Christopher J, Chang H, Tamir S, Hou B, Shacham S, Kauffman MG, Tripp RA, Landesman Y. 2021. Selinexor, a novel selective inhibitor of nuclear export, reduces SARS-CoV-2 infection and protects the respiratory system *in vivo*. *Antiviral Res* **192:** 105115. doi:10.1016/j.antiviral.2021.105115

Kim G-W, Siddiqui A. 2021. Hepatitis B virus X protein recruits methyltransferases to affect cotranscriptional N6-methyladenosine modification of viral/host RNAs. *Proc Natl Acad Sci* **118:** e2019455118. doi:10.1073/pnas.2019455118

Kim D, Paggi JM, Park C, Bennett C, Salzberg SL. 2019. Graph-based genome alignment and genotyping with HISAT2 and HISAT-genotype. *Nat Biotechnol* **37:** 907–915. doi:10.1038/s41587-019-0201-4

Kim D, Lee J-Y, Yang J-S, Kim JW, Kim VN, Chang H. 2020. The architecture of SARS-CoV-2 transcriptome. *Cell* **181:** 914–921.e10. doi:10.1016/j.cell.2020.04.011

Laver JD, Ly J, Winn AK, Karaiskakis A, Lin S, Nie K, Benic G, Jaberi-Lashkari N, Cao WX, Khademi A, et al. 2020. The RNA-binding protein Rasputin/G3BP enhances the stability and translation of its target mRNAs. *Cell Rep* **30:** 3353–3367.e7. doi:10.1016/j.celrep.2020.02.066

Lawrence M, Gentleman R, Carey V. 2009. rtracklayer: an R package for interfacing with genome browsers. *Bioinformatics* **25:** 1841–1842. doi:10.1093/bioinformatics/btp328

Lee S, Cook D, Lawrence M. 2019. plyranges: a grammar of genomic data transformation. *Genome Biol* **20:** 4. doi:10.1186/s13059-018-1597-8

Li N, Hui H, Bray B, Gonzalez GM, Zeller M, Anderson KG, Knight R, Smith D, Wang Y, Carlin AF, et al. 2021. METTL3 regulates viral m^{6}A RNA

modification and host cell innate immune responses during SARS-CoV-2 infection. *Cell Rep* **35:** 109091. doi:10.1016/j.celrep.2021.109091
Lichinchi G, Zhao BS, Wu Y, Lu Z, Qin Y, He C, Rana TM. 2016. Dynamics of human and viral RNA methylation during Zika virus infection. *Cell Host Microbe* **20:** 666–673. doi:10.1016/j.chom.2016.10.002
Liu J, Xu Y-P, Li K, Ye Q, Zhou H-Y, Sun H, Li X, Yu L, Deng Y-Q, Li R-T, et al. 2021. The m^{6}A methylome of SARS-CoV-2 in host cells. *Cell Res* **31:** 404–414. doi:10.1038/s41422-020-00465-7
Lorè NI, De Lorenzo R, Rancoita PMV, Cugnata F, Agresti A, Benedetti F, Bianchi ME, Bonini C, Capobianco A, Conte C, et al. 2021. CXCL10 levels at hospital admission predict COVID-19 outcome: hierarchical assessment of 53 putative inflammatory biomarkers in an observational study. *Mol Med* **27:** 129. doi:10.1186/s10020-021-00390-4
Lu W, Tirumuru N, St. Gelais C, Koneru PC, Liu C, Kvaratskhelia M, He C, Wu L. 2018. N^6-Methyladenosine–binding proteins suppress HIV-1 infectivity and viral production. *J Biol Chem* **293:** 12992–13005. doi:10.1074/jbc.RA118.004215
Meyer KD, Saletore Y, Zumbo P, Elemento O, Mason CE, Jaffrey SR. 2012. Comprehensive analysis of mRNA methylation reveals enrichment in 3′ UTRs and near stop codons. *Cell* **149:** 1635–1646. doi:10.1016/j.cell.2012.05.003
Patil DP, Chen C-K, Pickering BF, Chow A, Jackson C, Guttman M, Jaffrey SR. 2016. m^{6}A RNA methylation promotes *XIST*-mediated transcriptional repression. *Nature* **537:** 369–373. doi:10.1038/nature19342
Ping X-L, Sun B-F, Wang L, Xiao W, Yang X, Wang W-J, Adhikari S, Shi Y, Lv Y, Chen Y-S, et al. 2014. Mammalian WTAP is a regulatory subunit of the RNA N6-methyladenosine methyltransferase. *Cell Res* **24:** 177–189. doi:10.1038/cr.2014.3
Quinlan AR, Hall IM. 2010. BEDTools: a flexible suite of utilities for comparing genomic features. *Bioinformatics* **26:** 841–842. doi:10.1093/bioinformatics/btq033
Ramírez F, Ryan DP, Grüning B, Bhardwaj V, Kilpert F, Richter Andreas S, Heyne S, Dündar F, Manke T. 2016. deepTools2: a next generation web server for deep-sequencing data analysis. *Nucleic Acids Res* **44:** W160–W165. doi:10.1093/nar/gkw257
Ran J, Yang Y, Li D, Liu M, Zhou J. 2015. Deacetylation of α-tubulin and cortactin is required for HDAC6 to trigger ciliary disassembly. *Sci Rep* **5:** 12917. doi:10.1038/srep12917
R Core Team. 2022. *R: a language and environment for statistical computing*. R Foundation for Statistical Computing, Vienna. https://www.R-project.org/.
Ringlander J, Olausson J, Nyström K, Härnqvist T, Jakobsson HE, Lindh M. 2021. Recurrent and persistent infection with SARS-CoV-2: epidemiological data and case reports from Western Sweden, 2020. *Infect Dis* **53:** 900–907. doi:10.1080/23744235.2021.1957143
Riva L, Yuan S, Yin X, Martin-Sancho L, Matsunaga N, Pache L, Burgstaller-Muehlbacher S, De Jesus PD, Teriete P, Hull MV, et al. 2020. Discovery of SARS-CoV-2 antiviral drugs through large-scale compound repurposing. *Nature* **586:** 113–119. doi:10.1038/s41586-020-2577-1
Robinot R, Hubert M, de Melo GD, Lazarini F, Bruel T, Smith N, Levallois S, Larrous F, Fernandes J, Gellenoncourt S, et al. 2021. SARS-CoV-2 infection induces the dedifferentiation of multiciliated cells and impairs mucociliary clearance. *Nat Commun* **12:** 4354. doi:10.1038/s41467-021-24521-x
Roundtree IA, Luo G-Z, Zhang Z, Wang X, Zhou T, Cui Y, Sha J, Huang X, Guerrero L, Xie P, et al. 2017. YTHDC1 mediates nuclear export of N^6-methyladenosine methylated mRNAs. *eLife* **6:** e31311. doi:10.7554/eLife.31311
Saccon E, Chen X, Mikaeloff F, Rodriguez JE, Szekely L, Vinhas BS, Krishnan S, Byrareddy SN, Frisan T, Végvári Á, et al. 2021. Cell-type-resolved quantitative proteomics map of interferon response against SARS-CoV-2. *iScience* **24:** 102420. doi:10.1016/j.isci.2021.102420
Samelson AJ, Tran QD, Robinot R, Carrau L, Rezelj VV, Kain AM, Chen M, Ramadoss GN, Guo X, Lim SA, et al. 2022. BRD2 inhibition blocks SARS-CoV-2 infection by reducing transcription of the host cell receptor ACE2. *Nat Cell Biol* **24:** 24–34. doi:10.1038/s41556-021-00821-8
Schmidt N, Lareau CA, Keshishian H, Ganskih S, Schneider C, Hennig T, Melanson R, Werner S, Wei Y, Zimmer M, et al. 2021. The SARS-CoV-2 RNA–protein interactome in infected human cells. *Nat Microbiol* **6:** 339–353. doi:10.1038/s41564-020-00846-z
Somasekharan SP, Zhang F, Saxena N, Huang JN, Kuo I-C, Low C, Robert B, Adomat H, Stoynov N, Foster L, et al. 2020. G3BP1-linked mRNA partitioning supports selective protein synthesis in response to oxidative stress. *Nucleic Acids Res* **48:** 6855–6873. doi:10.1093/nar/gkaa376
Su R, Dong L, Li Y, Gao M, He PC, Liu W, Wei J, Zhao Z, Lei G, Han L, et al. 2022. METTL16 exerts an m^{6}A-independent function to facilitate translation and tumorigenesis. *Nat Cell Biol* **24:** 205–216. doi:10.1038/s41556-021-00835-2
Sun H, Li K, Zhang X, Liu J, Zhang M, Meng H, Yi C. 2021. m^{6}Am-seq reveals the dynamic m^{6}Am methylation in the human transcriptome. *Nat Commun* **12:** 4778. doi:10.1038/s41467-021-25105-5
Tao K, Tzou PL, Nouhin J, Gupta RK, de Oliveira T, Kosakovsky Pond SL, Fera D, Shafer RW. 2021. The biological and clinical significance of emerging SARS-CoV-2 variants. *Nat Rev Genet* **22:** 757–773. doi:10.1038/s41576-021-00408-x
Tarasov A, Vilella AJ, Cuppen E, Nijman IJ, Prins P. 2015. Sambamba: fast processing of NGS alignment formats. *Bioinformatics* **31:** 2032–2034. doi:10.1093/bioinformatics/btv098
Wang J, Shi C, Xu Q, Yin H. 2021. SARS-CoV-2 nucleocapsid protein undergoes liquid-liquid phase separation into stress granules through its N-terminal intrinsically disordered region. *Cell Discov* **7:** 5. doi:10.1038/s41421-020-00240-3
Wei G, Almeida M, Pintacuda G, Coker H, Bowness JS, Ule J, Brockdorff N. 2021a. Acute depletion of METTL3 implicates N^6-methyladenosine in alternative intron/exon inclusion in the nascent transcriptome. *Genome Res* **31:** 1395–1408. doi:10.1101/gr.271635.120
Wei J, Alfajaro MM, DeWeirdt PC, Hanna RE, Lu-Culligan WJ, Cai WL, Strine MS, Zhang S-M, Graziano VR, Schmitz CO, et al. 2021b. Genome-wide CRISPR screens reveal host factors critical for SARS-CoV-2 infection. *Cell* **184:** 76–91.e13. doi:10.1016/j.cell.2020.10.028
Wei J, Yu X, Yang L, Liu X, Gao B, Huang B, Dou X, Liu J, Zou Z, Cui X-L, et al. 2022. FTO mediates LINE1 m^{6}A demethylation and chromatin regulation in mESCs and mouse development. *Science* **376:** 968–973. doi:10.1126/science.abe9582
Wu F, Zhao S, Yu B, Chen Y-M, Wang W, Song Z-G, Hu Y, Tao Z-W, Tian J-H, Pei Y-Y, et al. 2020. A new coronavirus associated with human respiratory disease in China. *Nature* **579:** 265–269. doi:10.1038/s41586-020-2008-3
Xiao W, Adhikari S, Dahal U, Chen Y-S, Hao Y-J, Sun B-F, Sun H-Y, Li A, Ping X-L, Lai W-Y, et al. 2016. Nuclear m^{6}A reader YTHDC1 regulates mRNA splicing. *Mol Cell* **61:** 507–519. doi:10.1016/j.molcel.2016.01.012
Yamada T, Sato S, Sotoyama Y, Orba Y, Sawa H, Yamauchi H, Sasaki M, Takaoka A. 2021. RIG-I triggers a signaling-abortive anti-SARS-CoV-2 defense in human lung cells. *Nat Immunol* **22:** 820–828. doi:10.1038/s41590-021-00942-0
Yankova E, Blackaby W, Albertella M, Rak J, de Braekeleer E, Tsagkogeorga G, Pilka ES, Aspris D, Leggate D, Hendrick AG, et al. 2021. Small-molecule inhibition of METTL3 as a strategy against myeloid leukaemia. *Nature* **593:** 597–601. doi:10.1038/s41586-021-03536-w
Yue Y, Liu J, Cui X, Cao J, Luo G, Zhang Z, Cheng T, Gao M, Shu X, Ma H, et al. 2018. VIRMA mediates preferential m^{6}A mRNA methylation in 3′UTR and near stop codon and associates with alternative polyadenylation. *Cell Discov* **4:** 10. doi:10.1038/s41421-018-0019-0
Zaccara S, Ries RJ, Jaffrey SR. 2019. Reading, writing and erasing mRNA methylation. *Nat Rev Mol Cell Biol* **20:** 608–624. doi:10.1038/s41580-019-0168-5
Zeng Y, Wang S, Gao S, Soares F, Ahmed M, Guo H, Wang M, Hua JT, Guan J, Moran MF, et al. 2018. Refined RIP-seq protocol for epitranscriptome analysis with low input materials. *PLoS Biol* **16:** e2006092. doi:10.1371/journal.pbio.2006092
Zhang M-Z, Mai W, Li C, Cho S-Y, Hao C, Moeckel G, Zhao R, Kim I, Wang J, Xiong H, et al. 2004. PKHD1 protein encoded by the gene for autosomal recessive polycystic kidney disease associates with basal bodies and primary cilia in renal epithelial cells. *Proc Natl Acad Sci* **101:** 2311–2316. doi:10.1073/pnas.0400073101
Zhang Y, Liu T, Meyer CA, Eeckhoute J, Johnson DS, Bernstein BE, Nusbaum C, Myers RM, Brown M, Li W, et al. 2008. Model-based Analysis of ChIP-seq (MACS). *Genome Biol* **9:** R137. doi:10.1186/gb-2008-9-9-r137
Zhang S, Zhao BS, Zhou A, Lin K, Zheng S, Lu Z, Chen Y, Sulman EP, Xie K, Bögler O, et al. 2017. m^{6}A demethylase ALKBH5 maintains tumorigenicity of glioblastoma stem-like cells by sustaining FOXM1 expression and cell proliferation program. *Cancer Cell* **31:** 591–606.e6. doi:10.1016/j.ccell.2017.02.013
Zhang K, Miorin L, Makio T, Dehghan I, Gao S, Xie Y, Zhong H, Esparza M, Kehrer T, Kumar A, et al. 2021a. Nsp1 protein of SARS-CoV-2 disrupts the mRNA export machinery to inhibit host gene expression. *Sci Adv* **7:** eabe7386. doi:10.1126/sciadv.abe7386
Zhang X, Hao H, Ma L, Zhang Y, Hu X, Chen Z, Liu D, Yuan J, Hu Z, Guan W. 2021b. Methyltransferase-like 3 modulates severe acute respiratory syndrome coronavirus-2 RNA N6-methyladenosine modification and replication. *mBio* **12:** e0106721. doi:10.1128/mBio.01067-21
Zheng Z-Q, Wang S-Y, Xu Z-S, Yu-Zhi F, Wang Y-Y. 2021. SARS-CoV-2 nucleocapsid protein impairs stress granule formation to promote viral replication. *Cell Discov* **7:** 38. doi:10.1038/s41421-021-00275-0

Received November 20, 2021; accepted in revised form February 17, 2023.

Global loss of cellular m^{6}A RNA methylation following infection with different SARS-CoV-2 variants

Roshan Vaid, Akram Mendez, Ketan Thombare, et al.

Genome Res. published online March 1, 2023
Access the most recent version at doi:10.1101/gr.276407.121

Supplemental Materials for

Global loss of cellular m^{6}A RNA methylation following infection with different SARS-CoV-2 variants

Vaid, Mendez, *et al*

Department of Clinical Chemistry and Transfusion Medicine, Sahlgrenska University Hospital,

Gothenburg University, Gothenburg, Sweden.

Contents

Other Supplementary Materials for this manuscript

Supplemental Data S1: Differentially expressed genes following SARS-CoV-2 infection in Vero and HBE cells

Supplemental Data S2: Enrichment analysis of differentially expressed genes following SARS-CoV-2 infection in Vero and HBE cells.

Supplemental Data S3: m^{6}A peaks in the SARS-CoV-2 viral genome and in the host genomes of Noninfected and SARS-CoV-2 infected Vero, HBE, and HNE.

Supplemental Data S4: Genes with differential exon usage (DEU) in SARS-CoV-2 infected Vero cells.

Supplemental Figure S1

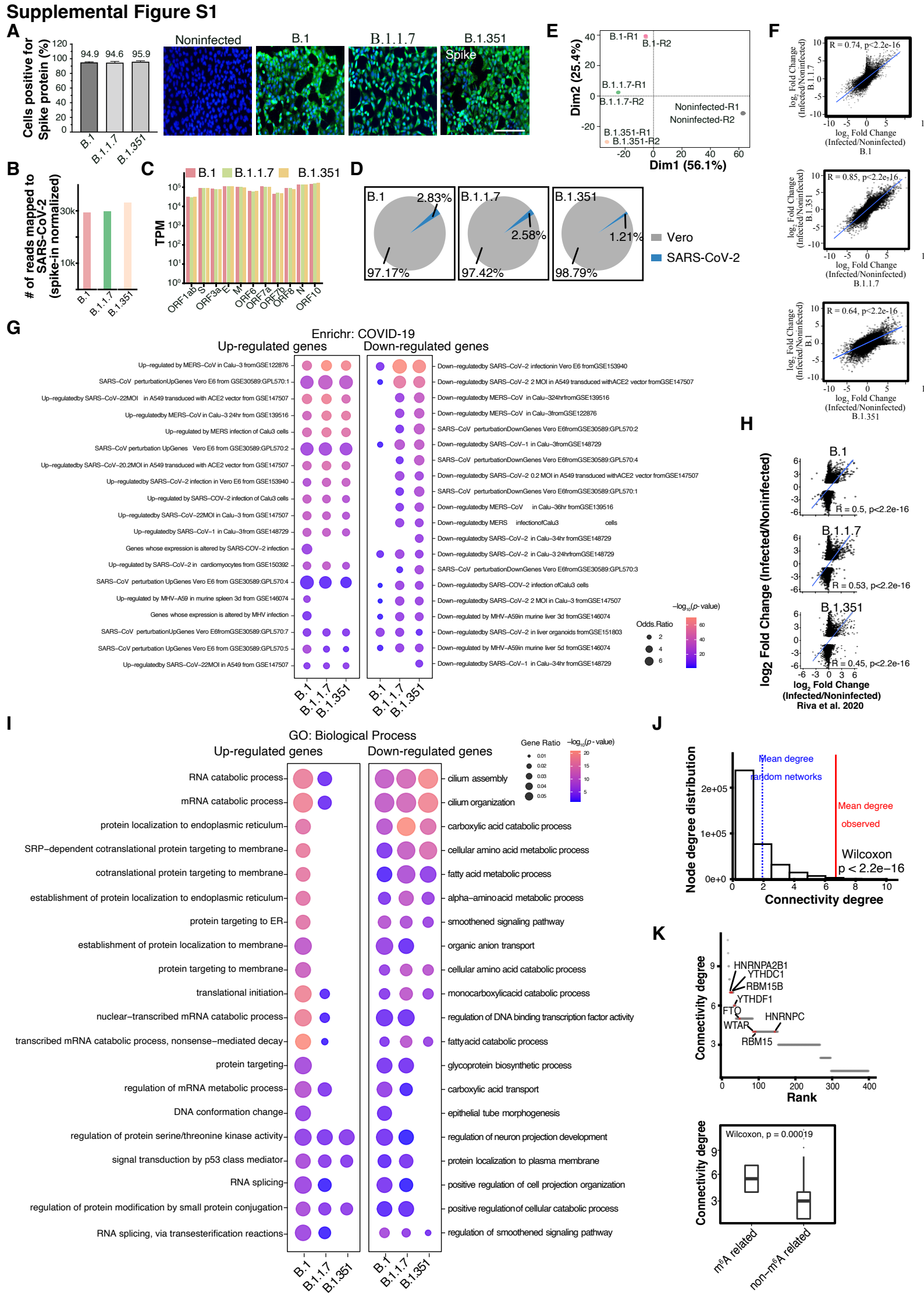

Supplemental_Figure_S1 (A) SARS-CoV-2 Spike protein staining summarized as bar plots with mean ± SD shown (left panel; n=2) and corresponding representative images of Spike staining (right panel) in Vero cells 48 h post-infection with three different SARS-CoV-2 variants as indicated. The scale bar is 200 μm. (B) Bar plots showing spike-in normalized reads mapped to the SARS-CoV-2 genome in Vero cells infected with different variants of SARS- CoV-2. (C) The $\log_{10}$ transcripts per million (TPM) values for SARS-CoV-2 genes in B.1, B.1.1.7, and B.1.351 infected cells. Data shown as the mean of two replicates. (D) Pie chart showing the percentage of reads mapping to host (Vero) and viral (SARS-CoV-2) genomes. (E) Principal-component analysis (PCA) of global expression patterns of SARS-CoV-2 infected (variants as specified) and noninfected Vero cells. Replicates are labelled with R1 and R2 suffixes. (F) Scatter plots showing correlation between $\log_2$ fold changes in gene expression after infection with different SARS-CoV-2 variants in Vero cells. Statistics: Pearson's correlation test. The blue line shows the linear regression with 95% confidence interval. (G) Top enriched terms associated with up-regulated and down-regulated genes after SARS-CoV-2 infection, based on publicly available COVID-19 related gene sets. Data were obtained from the Enrichr database. (H) Scatter plots of differentially expressed genes depicting the correlation between the $\log_2$ fold changes in gene expression after B.1, B.1.1.7, and B.1.351 infection and the $\log_2$ fold changes reported in publicly available data of SARS- CoV-2 infected Vero cells 24-hour post infection (Riva et al., 2020). The blue line depicts the linear regression line with 95% confidence interval. Statistics: Pearson's correlation test. (I) Top GO biological process terms associated with up-regulated and down-regulated genes after infection of Vero cells with the B.1, B.1.1.7, and B.1.351 strains. The size of the dots represents the enrichment of genes for a given GO term; the dots are colored according to their significance in $\log_{10}$ *p*-value. (J) Node connectivity degree distribution of 1000 randomly generated networks of the same size. The mean connectivity of random networks (blue dotted line) was compared to the observed mean connectivity degree of the network obtained after ClueGO analysis for RNA catabolism-associated genes (red line). Statistical significance was calculated using the Wilcoxon signed rank test. (K, top panel) Ranking of nodes according to their connectivity degree, with m^6A-related proteins highlighted in red. (K, bottom panel) Connectivity of m^6A-related proteins compared to other proteins in the network. Statistical significance was calculated using the Wilcoxon test.

Supplemental Figure S2

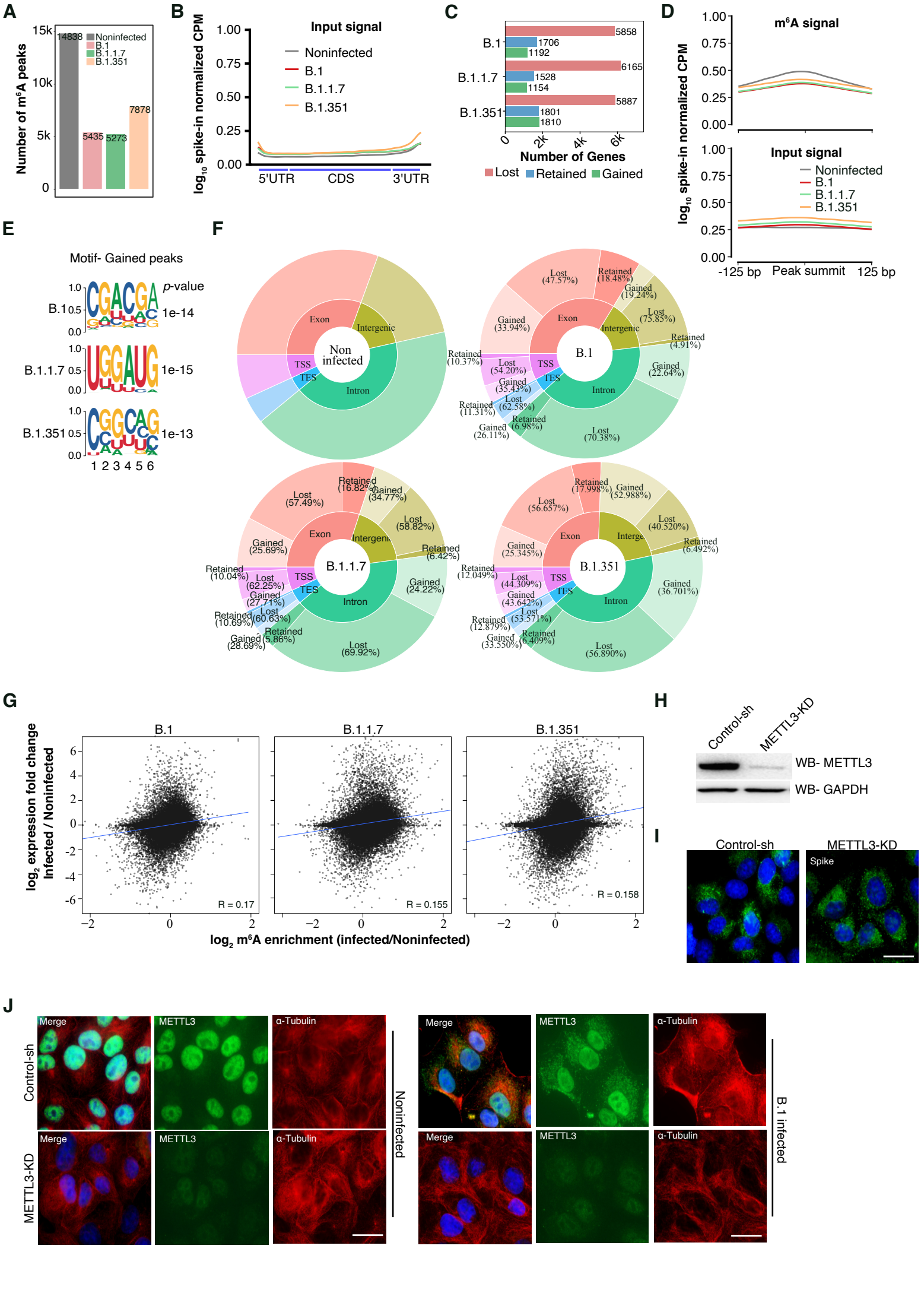

Supplemental Figure S2

K

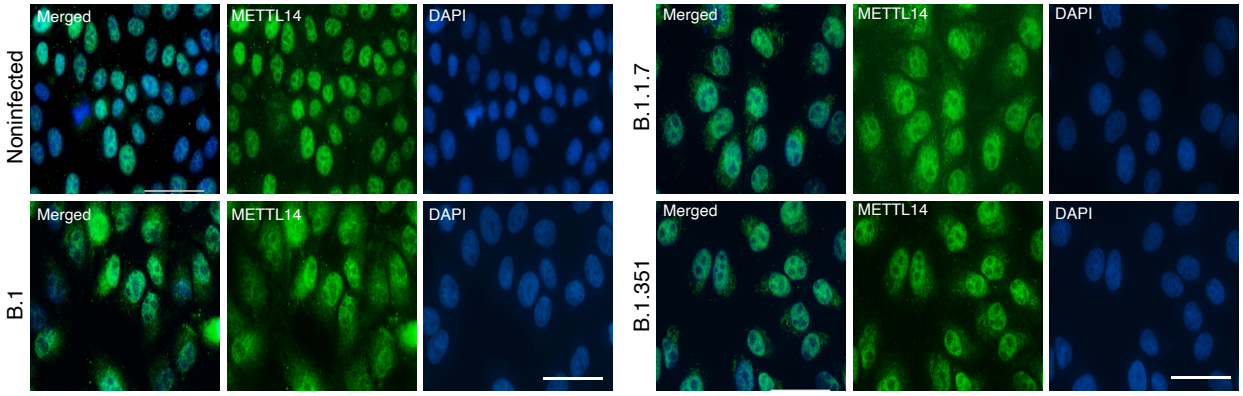

Supplemental_Figure_S2 (A) Number of m^6A peaks in Noninfected and infected Vero cells. (B) Metagene plot showing log_{10} spike-in normalized CPM of Input signals in the saples indiacted. (C) Bar plots representing the number of genes with lost, gained, or retained m^6A peaks in Vero cells after infection with three different SARS-CoV-2 variants, as indicated. (D) log_{10} spike-in normalized CPM of m^6A signal (top panel) and the corresponding input signal (bottom panel) at the m^6A peak regions (± 125bp from m^6A peak summit) that were commonly lost post- infection with the three different variants of SARS-CoV-2 compared to noninfected Vero cells. (E) Identified motifs from *de novo* motif analysis of gained m^6A peaks. Motifs from Vero cells infected with B.1, B.1.1.7, and B.1.351 are shown. (F) Donut plot distribution of annotated m^6A peaks by genomic features for noninfected and infected Vero cells with three different variants, as indicated. The proportion of retained, gained, and lost m^6A peaks annotated in exonic, intronic, transcription start site (TSS), transcription end site (TES), and intergenic regions are shown. (G) Scatter plots depicting the correlation between log_2 fold changes in gene expression and log_2 fold changes in m^6A enrichment after infection with B.1, B.1.1.7, and B.1.351 variants. The blue line depicts linear regression line with 95% confidence interval. Statistics: Pearson's correlation test. (H) Western-blot validation of METTL3 knock-down in Vero cells, with GAPDH used as a loading control. (I) Immunostaining using Spike antibody in control and METTL3-KD cells 48 h post SARS-CoV-2 infection. The scale bar is 20 μm (J) Immunostaining for METTL3 and α-Tubulin in Control and METTL3-KD Vero cells that were either Noninfected or infected with the B.1 SARS-CoV-2 variant. The scale bar is 20 μm (K) Immunostaining showing METTL14 localization in noninfected and Vero cells infected with the B.1, B.1.1.7, B.1.351 variants at 24h. The scale bar is 50 μm.

Supplemental Figure S3

A

Sample	Expected ratio A/m6A	Transition A	Transition m6A	Ratio A/m6A	Average ratio	Avg. number of m6A in 8954 Adenine in viral genome
Standard 1	5	2.26e+05	4.38e+04	5.2		
Standard 2	5	2.30e+05	3.59e+04	6.4	5.4	N/A
Standard 3	5	2.32e+05	4.87e+04	4.8		
SARS-CoV-2 B.1 Exp1	N/A	4.26e+07	6.09e+04	698.7		
SARS-CoV-2 B.1 Exp2	N/A	4.45e+07	4.41e+04	1,008.0	832.0	10.75* +/-1.98
SARS-CoV-2 B.1 Exp3	N/A	3.87e+07	4.89e+04	790.3		

B

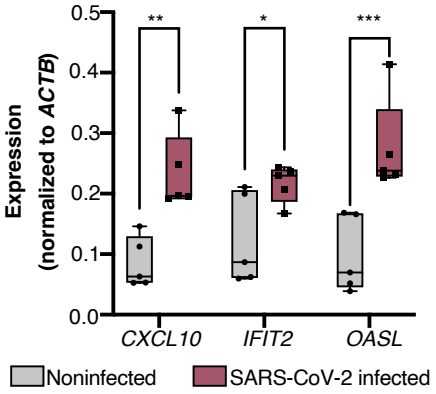

C

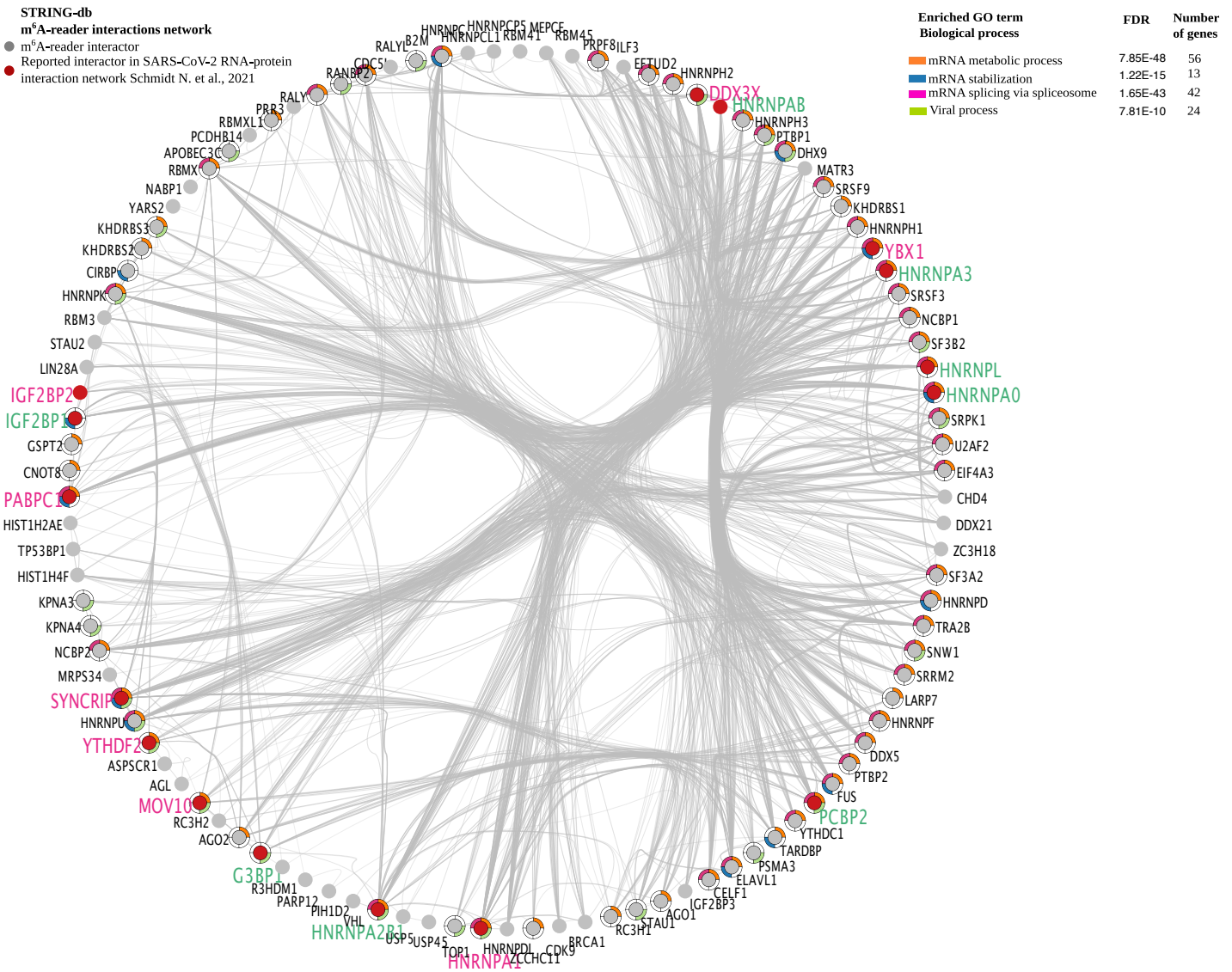

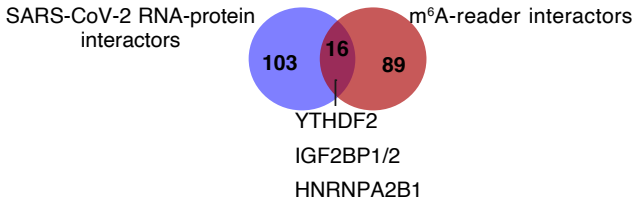

Supplemental_Figure_S3 (A) Summary of LC-MS/MS quantification of m^6A in control standard RNA oligos and B.1 viral genomic RNA. The average ratio of A/ m^6A in the viral genomic RNA was 832. Considering the total number of 'A' in the viral genome to be 8954, the number of 'A' with m^6A modification is on average 10.75 per viral genome. (B) RT-qPCR expression data (normalized to *ACTB*) of three selected genes in RNA isolated from throat/nose swab samples who were either positive (SARS-CoV-2 infected) or negative (noninfected) for COVID-19. (C) Interaction network of m^6A-related proteins. (Top panel) Interaction network of m^6A-related proteins. Known m^6A-reader interacting proteins collected from the STRING- db (grey nodes) were matched with the SARS-CoV-2 RNA-protein interactome obtained from Schmidt et al., 2020 (red nodes). The m^6A-related proteins pertaining to the core or the expanded SARS-CoV-2 interactome (as reported by Schmidt et al., 2021) labeled in pink and green, respectively. Outer node colors indicate enriched GO biological process terms for the m^6A-related proteins of the network. (Bottom panel) The Venn diagram shows the number of overlapping proteins between two datasets as indicated.

Supplemental Figure S4

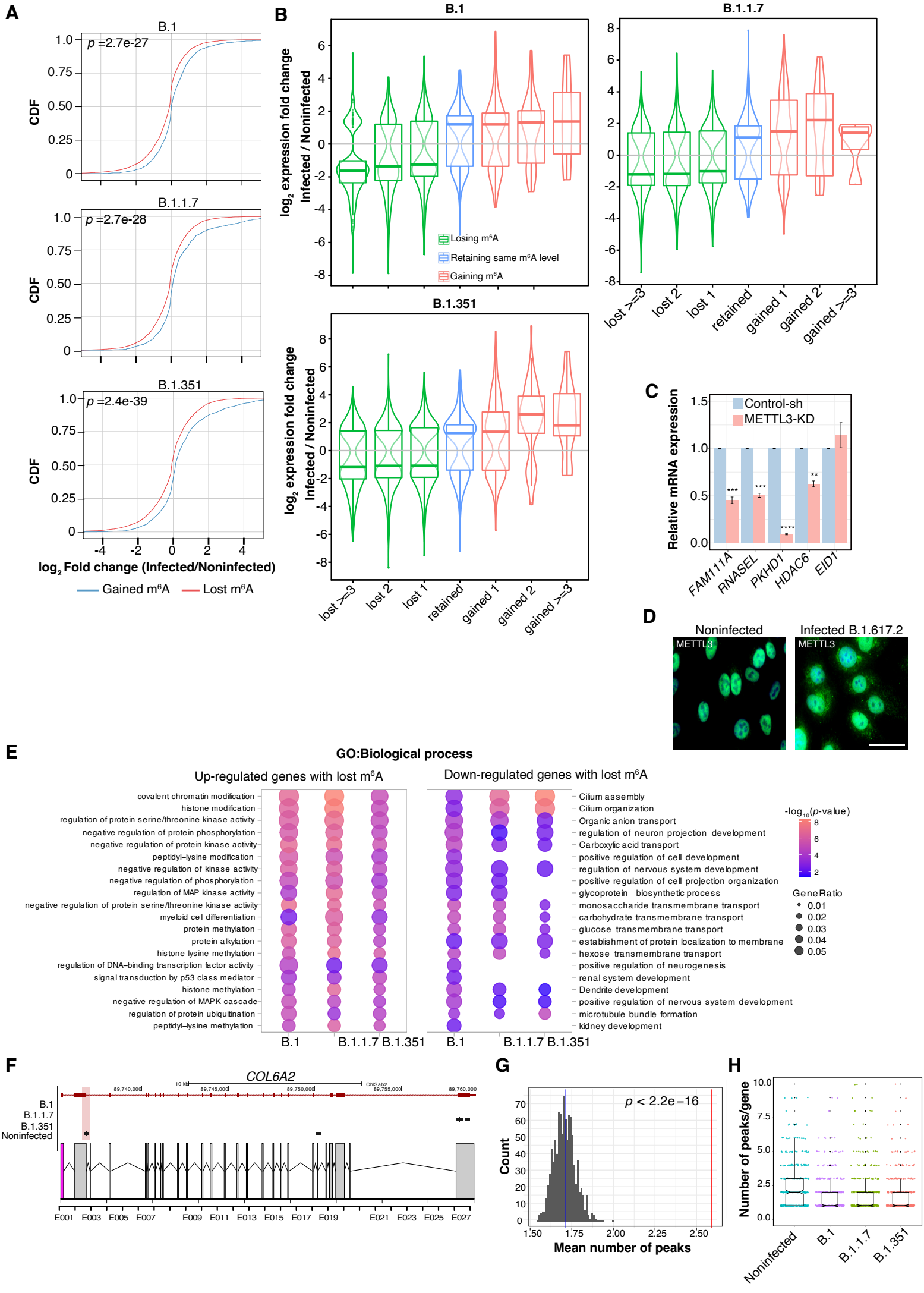

Supplemental_Figure_S4 (A) Cumulative distribution function (CDF) plots showing the cumulative density distribution of $\log_2$ fold changes in gene expression, with a comparison of lost (red) and gained (blue) m^{6}A genes after infection with different SARS-CoV-2 variants. Statistical significance was calculated using the Wilcoxon test. (B) Expression of m^{6}A-modified genes after SARS-CoV-2 infection. The distribution of differentially expressed genes categorized according to changes in m^{6}A levels after viral infection compared to Noninfected cells is shown. Genes were categorized as gaining one or more peaks (non- m^{6}A genes in non-infected cells being m^{6}A -modified after infection), losing one or more peaks (m^{6}A -modified genes in Noninfected cells showing a decrease in m^{6}A peak number), or retaining m^{6}A (showing the same number of m^{6}A peaks in noninfected and infected cells). (C) Relative expression of selected genes with varying levels of m^{6}A modification in METTL3-KD Vero cells compared to control cells. Data was normalized to *GAPDH* expression. Statistics: two- tailed *t*-test; **: $p < 0.01$, ***: $p < 0.001$, ****: $p < 0.0001$, n=3. (D) METTL3 localization in Vero cells infected with the B.1.617.2 (Delta) variant. The scale bar is 50 μm. (E) Top enriched terms associated with up-regulated and down-regulated genes with lost m^{6}A upon infection. The size of the dots depicts the gene enrichment ratio, while their color indicates the $\log_{10}$ level of significance. (F) Differential exon usage for the *COL6A2* gene upon SARS-CoV-2 infection. The genome browser visualization (top) shows the localization of m^{6}A peaks in noninfected and infected cells along the *COL6A2* gene. The exon structure (bottom) with a predicted differentially used exon (DEU) (in pink) included after infection is shown. (G) Distribution of the number of m^{6}A peaks over DEU genes compared to a random distribution in m^{6}A positive genes (1000 replicates without replacement). The average number of m^{6}A peaks in DEU genes and in m^{6}A positive random genes are denoted by a red and blue line, respectively. Statistics: one sample *t*-test. (H) Distribution of m^{6}A peak numbers in DEU genes in noninfected and infected Vero cells (infection with different variants as indicated).

Supplemental Figure S5

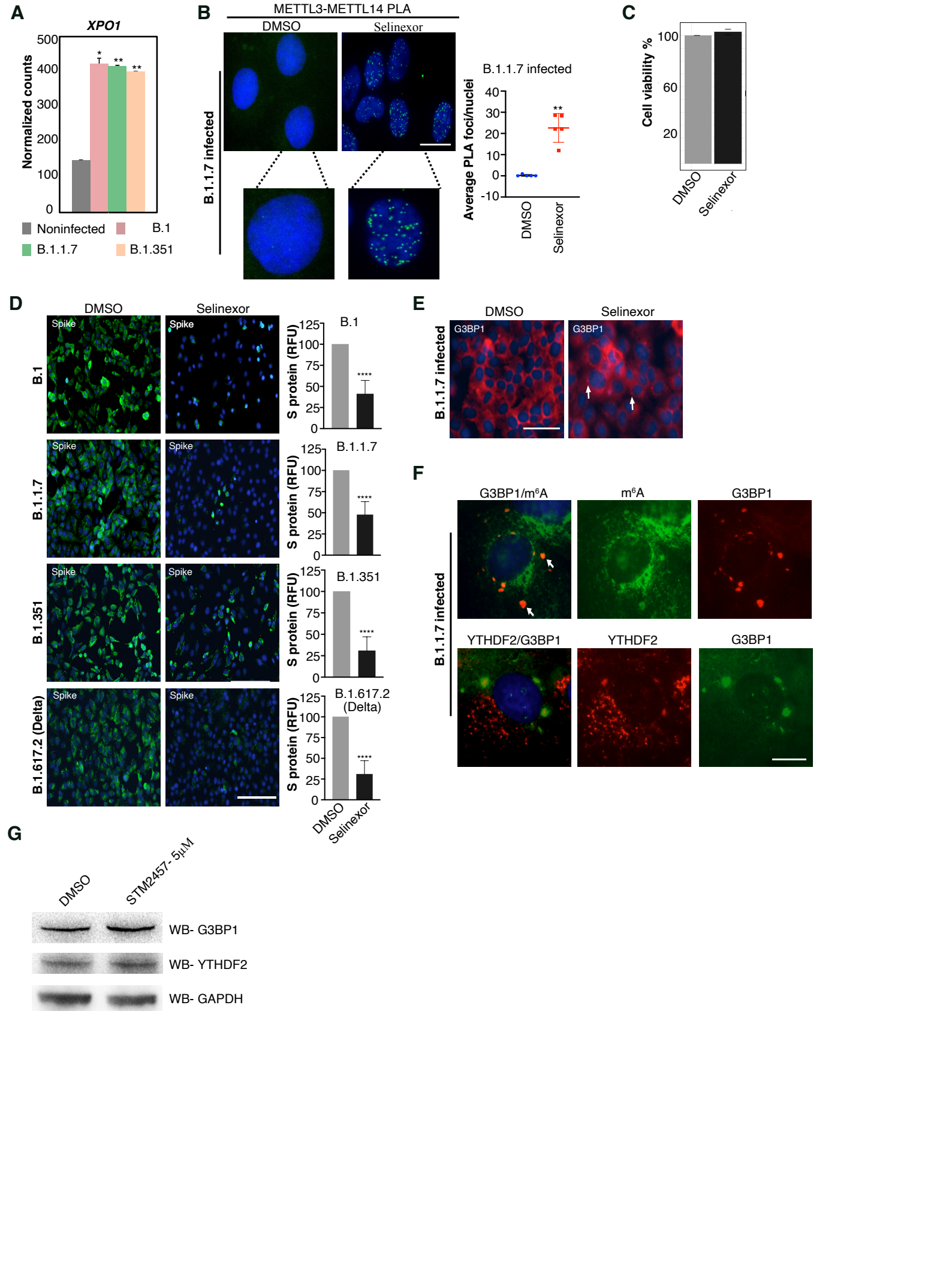

Supplemental_Figure_S5 (A) Bar graph depicting the expression of *XPO1* after infection with the B.1, B.1.1.7, and B.1.351 variants. Normalized read counts in RNA-seq data are reported. (B, left panel) PLA experiment revealing METTL3 and METTL14 interaction foci in the nucleus (marked by DAPI) of Vero cells infected with the B.1.1.7 variant and treated with either DMSO or Selinexor (150nM). The scale bar is 20 μm. (B, right panel) Quantification of METTL3-METTL14 PLA foci as detected in the left panel. The number of PLA foci/nuclei are shown as Mean ± SD. Data presented from multiple experiments with the total number of cells counted ≥100. Statistics: one-way ANOVA, **: $p < 0.01$. (C) MTT assay showing Vero cell viability after Selinexor treatment compared to DMSO control. (D, left) Immunostaining showing SARS-CoV-2 Spike protein in Vero cells at 48 h post-infection with the B.1, B.1.1.7, and B.1.617.2 (Delta) variants, with or without Selinexor treatment. (D, right) Quantification of Spike protein fluorescence in Selinexor-treated and untreated cells infected with different variants, as indicated. Spike fluorescence was quantified in 5 different fields obtained from several experiments. The scale bar is 200 μm. (E) Immunostaining showing G3BP1 localization after Selinexor treatment in B.1.1.7-infected cells at 24 h post-infection. White arrows highlight some of the G3BP1 foci. The scale bar is 50 μm. (F) Immunostaining showing the localization of G3BP1 and m^6A or YTHDF2 after DMSO or Selinexor treatment in B.1.1.7-infected cells at 24 h post-infection. White arrows highlight some of the G3BP1 foci overlapping with the m^6A signal. The scale bar is 10 μm. (G) Western blot detecting G3BP1 and YTHDF2 in Vero cells treated with STM2457 (5 μM) or DMSO. GAPDH was used as a loading control.

Supplemental Figure S6

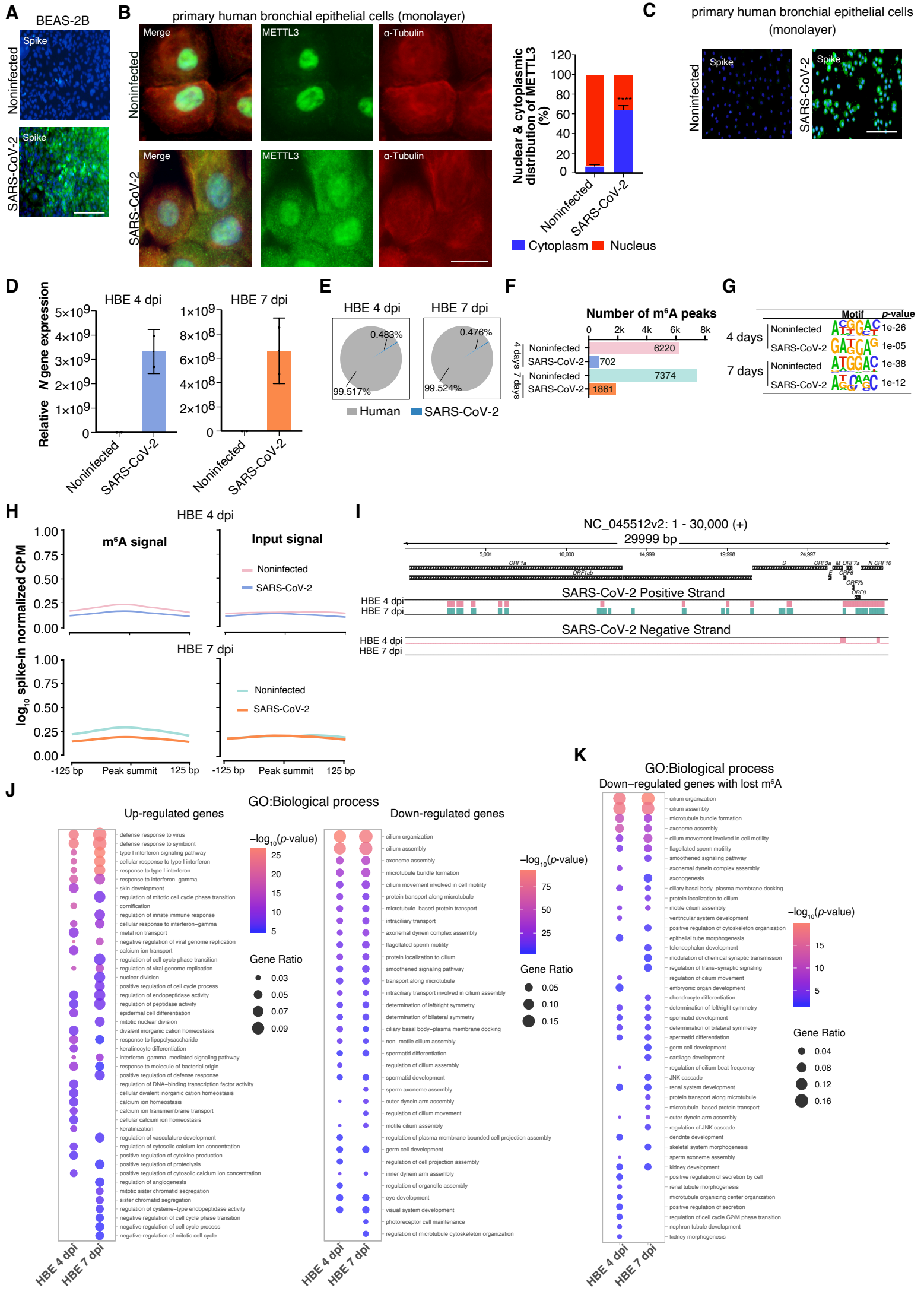

Supplemental_Figure_S6 (A) Spike immunostaining in BEAS-2B cells that were infected with SARS-CoV-2. The scale bar is 200 μm. (B, left panel) METTL3 localization in monolayer culture of Noninfected human primary bronchial epithelial cells and after infection with SARS-CoV-2. The scale bar is 20 μm. (B, right panel) The percentage distribution of METTL3 labeling in the nucleus and cytoplasm was calculated with ImageJ, using DAPI as a nucleus marker and α-Tubulin as a cytoplasm marker. Data are shown as mean ± SD. Data were obtained from multiple experiments with the total number of cells counted ≥110. Statistics: unpaired *t*-test; ****: $p < 0.0001$. (C) Spike protein immunostaining in human primary bronchial epithelial cells grown in monolayer that were infected with SARS-CoV-2. The scale bar is 200 μm. (D) Relative expression of SARS-CoV-2 *N* gene in noninfected and SARS- CoV-2 infected HBE samples 4- and 7- dpi. (E) Pie chart showing the percentage of RNA-seq reads mapping to host (Human) and viral (SARS-CoV-2) genomes in infected HBE samples. (F) Bar plot depicting the number of m^6A peaks in noninfected and SARS-CoV-2 infected HBE at 4- and 7- dpi. (G) Motif analysis of the m^6A peaks in noninfected and infected HBE. (H) $\log_{10}$ spike-in normalized CPM of m^6A signal (left panel) and the corresponding input signal (right panel) at the m^6A peak regions (± 125bp from m^6A peak summit) that were lost in infected HBE at 4- dpi (top) and 7-dpi (bottom) compared to noninfected HBE. (I) Presence of m^6A in the positive and negative strands of the SARS-CoV-2 viral genome at 4- and 7- dpi HBE cells. m^6A peak regions are indicated as colored rectangles. (J) Top GO biological process terms associated with up-regulated and down-regulated genes in HBE at day 4- and 7- dpi with SARS-CoV-2. (K) Top enriched terms associated with lost m^6A genes that were down- regulated in HBE at day 4- and 7- dpi with SARS-CoV-2. (J, K) The size of the dots depicts the gene enrichment ratio, while the color of the dots indicates the $\log_{10}$ level of significance.

Supplemental Figure S7

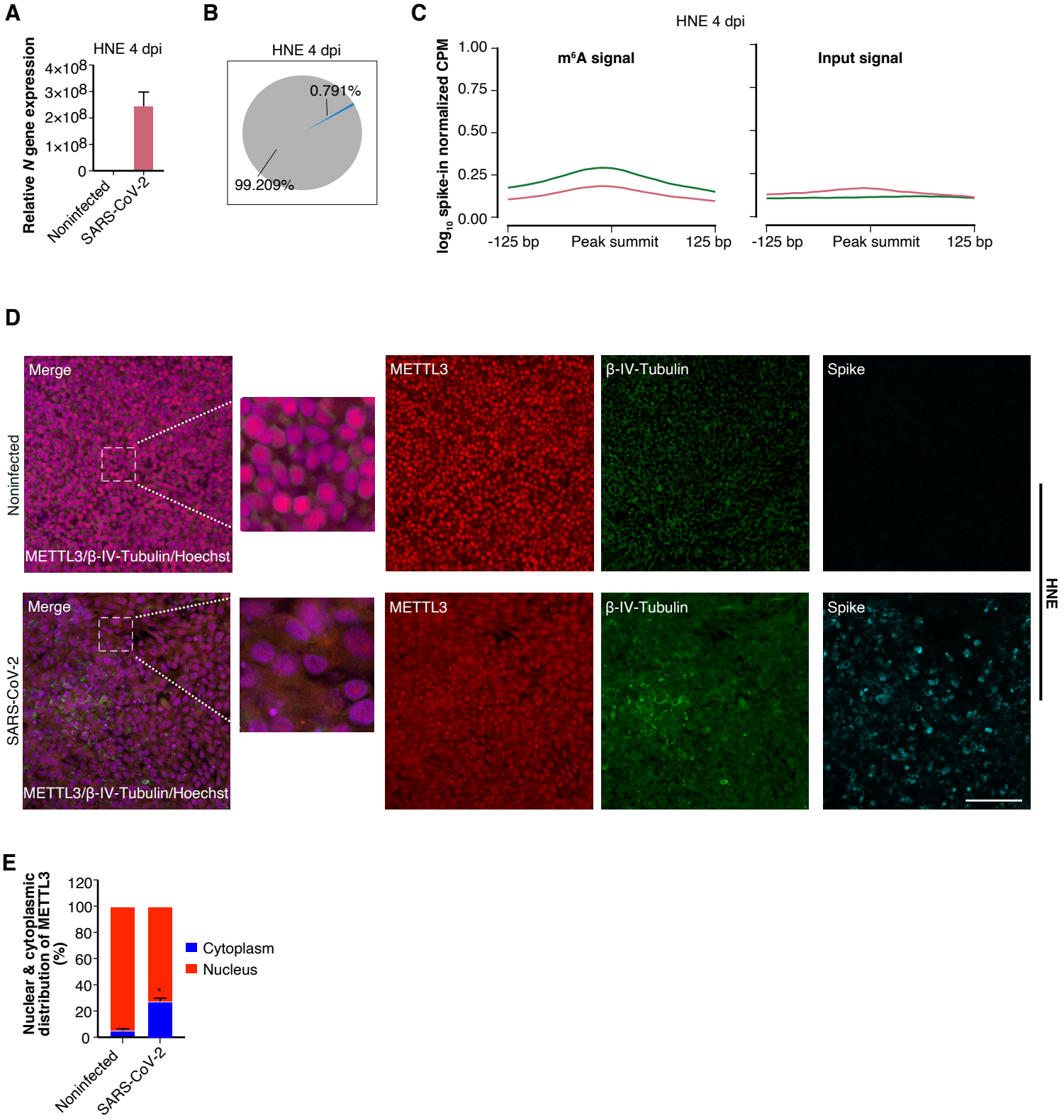

Supplemental_Figure_S7 (A) Relative expression of SARS-CoV-2 *N* gene in noninfected and SARS-CoV-2 infected HNE samples at 4- dpi. (B) Pie chart showing the percentage of reads mapping to the host (Human) and viral (SARS-CoV-2) genomes in infected HNE at 4- dpi. (C) $\log_{10}$ spike-in normalized CPM of m^6A signal (left panel) and the corresponding input signal (right panel) at the m^6A peak regions (± 125bp from m^6A peak summit) that were lost at 4- dpi in infected compared to noninfected HNE. (D) Immunostaining staining showing METTL3 (in red), β-IV-Tubulin (in green) and SARS-CoV-2 spike protein (in cyan) in HNE 4- dpi along with noninfected control. Merged image represents METTL3 and β-IV-Tubulin along with Hoechst. The scale bar is 200 μm. (E) The percentage distribution, of METTL3 in the nucleus and cytoplasm, was calculated using ImageJ. Hoechst was used as a nuclear marker and β-IV-Tubulin marking the cytoplasm. Data are shown as mean ± SD. Data were acquired from n=2 experiments with the total number of cells counted ≥ 1000. Statistics: unpaired t-test; ****: $p < 0.0001$.

Supplemental Tables

Supplemental Table S1: Sequence of oligos used in the study.

Vero		
Primer name	**Sequence**	
FAM111A-Forward primer	CCTTTCCTTCTGGCTCTTCA	
FAM111A-Reverse primer	TGTGGGAGACGGAATAGAGC	
HDAC6-Forward primer	CCCAATCTAGCGGAGGTAAA	
HDAC6-Reverse primer	CGCGATTAGGTCTTCTTCCA	
PKHD1-Forward primer	GTGGGCATTTGGTCTGAAAG	
PKHD1-Reverse primer	AGTTGTCCCAGCAGGACAGT	
RNASEL-Forward primer	TGTCAATGTGAGGGGAGAAA	
RNASEL-Reverse primer	CTTCACCAAACCCAAGTGCT	
EID1-Forward primer	TCGCCTCCTTTTTCACAACT	
EID1-Reverse primer	TGCCATTGAAAAACTTGACCT	
XPO1-Forward primer	TGGTACAGAATGGTCATGGAA	
XPO1-Reverse primer	TCTTCATGCATTGCTCCACT	
YTHDF1-Forward primer	TGGGACAAATGTGAACATGC	
YTHDF1-Reverse primer	TTTAGGCTGTGGTTTTGCAG	
FTO-Forward primer	GGAACCTTATTTTGGCATGG	
FTO-Reverse primer	GCTGACCTGTCCACCAGATT	
SPEN-Forward primer	CCACTCTCTCGGGATCAAAA	
SPEN-Reverse primer	AATCTCGTTTGGAGCGCTAT	
GAPDH-Forward primer	ATGTTCGTCATGGGTGTGAA	
GAPDH-Reverse primer	GGTGCTAAGCAGTTGGTGGT	
POL2RG- Forward primer	ACTGTTGGTGGGTGAGCAC	
POL2RG- Reverse primer	CCAGACTGGCAGCAAGAAAA	
TBP- Forward primer	ACTGTTGGTGGGTGAGCAC	
TBP- Reverse primer	CCAGACTGGCAGCAAGAAAA	
SARS-Cov-2		
Primer name	**Sequence**	
N-protein-Forward primer	CACATTGGCACCCGCAATC	
N-protein-Reverse primer	GAGGAACGAGAAGAGGCTTG	
N-Forward strand	CAGCACTGCTCATGGATTG	Primer for cDNA synthesis
N-Reverse strand	GACCCCAAAATCAGCGAAAT	Primer for cDNA synthesis
Human		
Primer name	**Sequence**	
CXCL10 Forward primer	TGATCTCAACACGTGGACAA	
CXCL10 Reverse primer	ACTGTACGCTGTACCTGCAT	

IFIT2 Forward primer	AAAGGAACCAGAGGCCACTT	
IFIT2 Reverse primer	GCTCGGTTCAGGCAGCTG	
OASL Forward primer	GGACTCTCTGCTCCATCCTC	
OASL Reverse primer	GCAGCCAAGCATCACAAAGA	
ACTB Forward primer	CTCGTAGCTCTTCTCCAGGG	
ACTB Reverse primer	GGGAAATCGTGCGTGACATT	
RNA standard for LC-MS/MS		
RNA oligo with m^6A	GGm^6ACUAAm^6ACU	
RNA oligo without m^6A	GGACUAAACU	
shRNA sequence		
METTL3 shRNA	GCTGCACTTCAGACGAATTAT	
Control shRNA	ATCTCGCTTGGGCGAGAGTAAG	

Supplemental Table S2: Scaling factor used for normalizing m^{6}A RIP data

Vero	
Sample	**Scaling factor**
Noninfected_m^{6}A RIP	1
B.1_m^{6}A RIP	0,72
B.1.7.7_m^{6}A RIP	0,81
B.1.351_m^{6}A RIP	0,98
Noninfected_Input	0,76
B.1_Input	0,76
B.1.7.7_Input	0,83
B.1.351_Input	1
HBE	
Sample	**Scaling factor**
HBE Noninfected day 4_m^{6}A RIP	0,75
HBE SARS-CoV-2 day 4_m^{6}A RIP	1
HBE Noninfected day 7_m^{6}A RIP	0,99
HBE SARS-CoV-2 day 7_m^{6}A RIP	1
HBE Noninfected day 4_Input	1
HBE SARS-CoV-2 day 4_Input	0,92
HBE Noninfected day 7_Input	0,94
HBE SARS-CoV-2 day 7_Input	1
HNE	
Sample	**Scaling factor**
HNE Noninfected_m^{6}A RIP	0,92
HNE SARS-CoV-2_m^{6}A RIP	1
HNE Noninfected_Input	0,67
HNE SARS-CoV-2_Input	1

Supplemental methods

Cell culture, SARS-CoV-2 infection and XPO1 inhibitor treatment

B.1 is the lineage with the D614G spike amino acid change. B.1.1.7 is the Alpha variant (WHO label) and the earliest documented variant in the UK (Sep-2020). B.1.1.351 is the Beta variant (WHO label) and was first documented in South Africa (May 2020). T25 flasks with Vero CCL-81 (ATCC) were infected with the three different SARS-CoV-2 variants (1000 $TCID_{50}$) and medium or infected cells were harvested in TRIzol 48 h post-infection for RNA-sequencing studies. In all cases, the amount of infection was verified by immunostaining and RT-qPCR (see method below). Vero CCL-81 cells were cultured in chamber slides and the different SARS-CoV-2 variants were diluted in medium to 1000 $TCID_{50}$ (DMEM with 1% penicillin-streptomycin and 2% fetal calf serum), supplemented with DMSO or Selinexor (150nM). 200 µl of the diluted virus was added to each well and the slides were incubated for 24 h at 37°C at 5% CO_2. The cells were fixed using 4% formaldehyde in PBS for 10 min at room temperature (RT) in chamber slides and washed three times in PBS.

Primary human bronchial epithelial cells (Lonza, CC-2540S) and bronchial epithelial cell line BEAS-2B (ATCC) were received as a gift from Professor Madeleine Rådinger group, Gothenburg University, Sweden, and were cultured in monolayer following manufacturer instructions. Primary human bronchial epithelial and BEAS-2B cells were infected with the B.1.1.7 variant of SARS-CoV-2 in a similar way to Vero cells as described above in their corresponding culture media and fixed using 4% formaldehyde in PBS for 10 min at RT in chamber slides 72 h post-infection.

SARS-CoV-2 infection of reconstructed human bronchial and nasal epithelia

MucilAir™ cultures, corresponding to reconstructed human bronchial and nasal epithelia (HBE and HNE, respectively) differentiated at the air/liquid interface (ALI), were purchased from Epithelix (Saint-Julien-en-Genevois, France). Cultures were maintained in ALI conditions in transwells with 700 µL of MucilAir™ medium (Epithelix) in the basal compartment and kept at 37°C under a 5% CO_2 atmosphere. SARS-CoV-2 infection was performed in epithelial cultures as previously described (Robinot et al. 2021). Briefly, the apical side of ALI cultures was washed once, and cells were then incubated with the isolate BetaCoV/France/IDF00372/2020 (EVAg collection, Ref-SKU: 014V-03890)

diluted in 150 µl of DMEM medium. The viral input was left on the apical side for 4 h at 37 °C, and then removed by 3 apical washes. Positivity for SARS-CoV-2 infection was tested by RT-qPCR as described below.

Immunofluorescence Staining

Cells were fixed with 4% formaldehyde for 10 min, followed by two washes with phosphate-buffered saline (PBS). Then cells were permeabilized using 0.25% Triton X-100 in PBS for 10 min followed by two washes with PBS-0.1% Tween 20 (PBST). Blocking was performed in 3% bovine serum albumin (BSA) in PBST for an hour at RT. The cells were incubated overnight at 4 °C with the following primary antibodies: anti-METTL3 rabbit antibody (1:300, ab195352; Abcam), anti-METTL14 rabbit antibody (1:300, HPA038002; Atlas Antibodies), anti-α-Tubulin mouse antibody (1:1000, T5168; Merck), anti-SARS-CoV-2 Spike glycoprotein rabbit antibody (1:300, ab272504; Abcam), anti-G3BP mouse antibody (1:500, ab56574; Abcam), anti-m^{6}A rabbit antibody (1:400, 202003, Synaptic Systems), and anti-YTHDF2 rabbit antibody (1:100, ab246514; Abcam). The slides were washed three times for 5 min in PBST and subsequently incubated with secondary antibodies conjugated with Alexa Fluor 488 and Alexa Fluor 555 fluorochromes (1:800; Invitrogen), for an hour in the dark at RT. After incubation with the secondary antibodies, cells were washed three times for 5 min in PBST. Prolong Gold with DAPI (Thermo Fisher Scientific–Life Technologies) was added to each coverslip and air-dried in the dark to detect nuclei. Slides were imaged in a fluorescence microscope (EVOS™ FL Auto, Thermo Fisher Scientific) using 20X and 60X oil immersion objectives by keeping the same parameter during image acquisition.

For immunofluorescence staining in HNE, MucilAir^{TM} cultures were fixed in 4% PFA for 30 mins at RT, washed two times with PBS, and cut using a scalpel blade. Membrane pieces were placed in 10 µl drops on parafilm, and subsequent staining steps were performed on parafilm at RT. Cells were permeabilized with 0.5% Triton X-100 in PBS for 20 min and then blocked in 0.1% Tween 20, 1% bovine serum albumin (BSA), 10% fetal bovine serum, 0.3 M glycine in PBS for 30 min. Samples were incubated overnight at 4°C with AF647 conjugated rabbit anti-METTL3 primary antibody (ab217109; Abcam; 1:100 dilution), AF488 conjugated rabbit anti-β-IV-Tubulin (ab204003; Abcam; 1:250 dilution) and anti-spike (1:100, is a gift from Hugo Mouquet (Pasteur Institute). The samples were

washed thrice in PBS followed by one hour incubated at RT with secondary antibody AF555-conjugated goat anti-mouse (1:500 dilution). Samples were counterstained with Hoechst and mounted in FluoromountG (Thermo Fisher Scientific) before observation with a Leica TCS SP8 confocal microscope (Leica Microsystems).

For quantification of METTL3 localization, images were analyzed with ImageJ. Fluorescence channels corresponding to the nuclear marker (DAPI/ Hoechst) and cytoplasmic marker (anti- α-Tubulin or anti-β-IV-Tubulin) were split to mark the nuclear and cytoplasmic border followed by quantification of METTL3 intensity (Relative Fluorescence Unit: RFU) in nucleus and cytoplasm.

RT-qPCR and m^{6}A RIP-qPCR

For performing m^{6}A RIP-qPCR, 3 µg of RNA from Vero cells infected with SARS-CoV-2 B.1.1.7 variant or human patient RNA samples from throat/nose swabs (ethical permit # 2020-03276, #2020-01945 and #2022-01139-02) were used. RIP was performed with 1µg of m^{6}A antibodies (synaptic systems, 202003) or IgG antibodies (SantaCruz, SC-2027). The input and m^{6}A RIP-RNA were converted to cDNA using the High-Capacity RNA-to-cDNA™ Kit (Thermo Fisher Scientific, 4387406) and random primers. qPCR was performed on a Quant Studio 3 thermocycler (Thermo Fisher Scientific) using gene-specific PCR primers (**Supplemental Table S1**) mixed with Power SYBR Green Master Mix (Thermo Fisher Scientific, 4367659) and diluted cDNA (10-fold dilution) as a template. The data is represented as percentage input values.

For RT-qPCR, the RNA was directly converted to cDNA and subjected to qPCR as mentioned above, using primers listed in Supplemental Table S1. Expression values presented for each gene are normalized to *TBP* and *POL2RG* or to *GAPDH* using the delta-delta Ct method.

To check m^{6}A levels in both forward and reverse strands of the viral RNA, cDNA was synthesized with primers specific for each strand separately at 50 °C (**Supplemental Table S1**) using the ImProm-II™ Reverse Transcription System (Promega, A3800) and subjected to qPCR with primers specific for the viral N-protein (**Supplemental Table S1**).

Human patient RNA samples from throat/nose swabs were converted to cDNA and subjected to qPCR as mentioned above, using primers listed in Supplemental Table S1. Expression was normalized to *ACTB*.

The cellular level of SARS-CoV-2 RNA was measured by RT-qPCR in HBE and HNE infection as described previously (Samelson et al. 2022).

G3BP1 and YTHDF2 RNA Immuno-precipitation qPCR (RIP-qPCR)

Uninfected Vero cells treated with the METTL3 inhibitor STM2457 (5μM for 48h) or with DMSO were harvested and fixed for 10 mins with formaldehyde (1% final concentration) and quenched with Glycine (0.125 M, final concentration). Fixed cells were lysed in RIPA buffer (50mM Tris pH7.4, 150mM NaCl, 0.5% Sodium Deoxycholate, 0.2% SDS, 1% IGEPAL-CA630, Protease inhibitor, and RNase inhibitor) and sonicated for 10 cycles (30 secs on 30 secs off) on a Bioruptor (Diagenode) sonicator. The cleared lysate was used for RIP with anti-G3BP1 (Abcam, Ab181150), anti-YTHDF2 (Abcam, Ab246514) and IgG (SantaCruz, SC-2027) antibodies. The RNA-protein-antibody complex was captured using protein A/G magnetic beads (Thermo Fisher Scientific, 10002D and 10004D). Magnetic beads were washed with low salt buffer (1X PBS, 0.1% SDS and 0.5% IGEPAL-CA630) and high salt buffer (5X PBS, 0.1% SDS and 0.5% IGEPAL-CA630) before eluting in elution buffer (10mM Tris pH7.4, 100mM NaCl, 1mM EDTA, 0.5% SDS) with Proteinase K. RNA was extracted using TRIzol reagent and cDNA synthesis and RT-qPCR were performed as described above. The data is represented as percentage input values.

LC-MS/MS quantification of m^6A in viral RNA

LC-MS/MS-based quantification of m^6A was done as previously described (Liu et al. 2021, 2020a). In brief, RNA from B.1 viral particles was isolated from Vero cell supernatant and digested by P1 nuclease (Sigma, N8630) followed by treatment with phosphatase (NEB, M0289S). The sample was then filtered (0.22 μm pore size) and directly injected into the LC-MS apparatus. As a positive standard for LC-MS/MS, and to estimate the number of m^6A modifications in viral RNA, we parallelly processed commercially synthesized RNA oligos (**Supplemental Table S1**) with or without internal m^6A mixed at a 5:1 A/m^6A ratio. We made triplicate injections of the standard RNA oligos and the viral RNA and estimated the A/m^6A ratios for both samples. LC-MS/MS profiles were monitored using the parallel reaction-monitoring (PRM) mode for: m/z 268.0–136.0, and m/z 282.0–150.1 that corresponds to A and m^6A respectively, as previously described (Sun et al. 2021).

METTL3 knock-down and Western blot analysis

Vero cells with stable METTL3 (METTL3-KD) and control knockdown (Control-sh) were generated using lentivirus expressing shRNA against METTL3 or non-targeting genomic regions. The shRNA sequences used in the study are provided in Supplemental Table S1.

Total proteins were extracted from cells using RIPA buffer (Sigma-Aldrich, #R0278) and quantified using the Pierce BCA Protein Assay Kit (Thermo Scientific, #23225) as per the manufacturer's instructions. An equal amount of proteins per sample were resolved by SDS- PAGE on NuPAGE Bis-Tris gels (4-12%) (Invitrogen), followed by transfer onto 0.2 μm Nitrocellulose membrane using a Trans-Blot Turbo Transfer System (Bio-Rad). The membrane was blocked for 1 h at RT with a blocking solution (PBST- 5%Milk) before incubation with the primary antibodies, anti-METTL3 (1:400, Ab195352; Abcam), anti-G3BP1 (1:1000, Abcam, Ab181150), anti-YTHDF2 (1:1000, Abcam, Ab246514) or anti-GAPDH (1:5000, ab9485, Abcam), in blocking solution overnight at 4°C. After washing, the membranes were incubated with a secondary antibody for 1 h at RT, and the proteins were then detected with the SuperSignal West Pico PLUS Chemiluminescent Substrate (Thermo Scientific, #34579) using a ChemiDoc XRS+ system (Bio-Rad).

Proliferation assay

5,000 cells/well were seeded in a 96-well plate to assess the proliferation of cells treated with either DMSO or Selinexor (150nM). The CellTiter 96 Non-Radioactive Cell Proliferation Assay kit (Promega, #G4000) was used to determine cell growth as per the manufacturer's instructions. Absorbance was measured using a microplate reader Infinite 50 (Tecan, Austria).

Excluding potential N6,2′-*O*-dimethyladenosine (m^6Am) signals

To evaluate the presence of potential m^6Am modification located at the first-transcribed nucleotide (Tan et al. 2018; Liu et al. 2020b), we bioinformatically excluded m^6A RIP-seq signals located near the transcription start sites (TSS) that could correspond to m^6Am modifications captured by the m^6A antibody. For this, the summit coordinates of predicted m^6A RIP-seq peaks were overlapped with the first 20 nt (close to transcription start sites) of all transcripts using the plyranges package (Lee et al. 2019) according to each reference genome (chlsab2, hg38 or wuhCor1). The m^6A peaks located within the 20 bp regions from transcription start sites were excluded from the analysis.

Quantification of viral reads

Counts of reads uniquely mapped to the SARS-CoV-2 genome were obtained with featureCounts (Liao et al. 2019) and normalized to the spike-in scaling factor. TPM values were then calculated using these counts by further normalizing with the gene lengths to obtain viral gene expression. Averaged TPM expression values were calculated for all replicates in Vero, HBE, and HNE post-infection samples, reflecting the different numbers of viral reads depending on the host cells.

Analysis of m^{6}A-readers from publicly available SARS-CoV-2 interactome

We collected publicly available data from the SARS-CoV-2 interactome in Schmidt et al., 2021 to analyze the reported interactions of known m^{6}A-readers. For this, we selected proteins with a significant $\log_2$ enrichment over the background. As reported by the original authors, the SARS-CoV-2 RNA-protein interactome can be further divided into a core (adjusted p-value < 0.05) and expanded interactome (adjusted p-value < 0.2), containing 57 and 119 RNA interacting proteins, respectively. After matching the significantly enriched SARS-CoV-2 RNA-protein interactome data with the publicly available m^{6}A-reader protein interactors collected from STRINGdb, we found 16 overlapping proteins. From these, 8 proteins belong to the core SARS-CoV-2 RNA-protein interactome (YTHDF2, YBX1, SYNCRIP, PABPC1, MOV10, DDX3X, HNRNPA1, and IGF2BP2) and 8 proteins (IGF2BP1, HNRNPA3, HNRNPA0, HNRNPAB, HNRNPL, G3BP1, PCBP2, and HNRNPA2B1) form part of the expanded SARS-CoV-2 interactome. The resulting interaction network was analyzed and visualized using StringApp Cytoscape plugin (Doncheva et al. 2019).

Analysis of RNA-seq data for differential gene expression

Aligned reads were quantified using featureCounts from the Rsubread package (Liao et al. 2019) following differential expression analysis with DESeq2 using two replicates per condition (Love et al. 2014). Genes were considered differentially expressed if they had an absolute $\log_2$ fold change value > 1 and an adjusted p-value cutoff of < 0.01 for Vero data and $\log_2$ fold change > 0.5 and adjusted p-value < 0.1 for HBE data. Heatmap visualization of differentially expressed genes was generated using the pheatmap package in R. Principal component analysis of gene expression patterns after infection with different SARS-CoV-2 variants was calculated on the regularized normalized counts obtained from DESeq2 using the factoextra package. Correlation analysis of the gene expression changes was

performed between cells infected with different SARS-CoV-2 variants and also at the level of differentially expressed genes in different infection conditions. Publicly available data were used as well (Riva et al. 2020). Functional enrichment analysis was carried out using clusterProfiler (Yu et al. 2012) or Enrichr (Chen et al. 2013) against the Gene Ontology biological process or Enrichr COVID-19 related gene sets databases, respectively, with the selection of significantly enriched terms (*p*-value < 0.05). GO term clustering and visualization analysis was carried out using ClueGO (Bindea et al. 2013) from Cytoscape v3.8.2. Briefly, common enriched terms across any pair of variants previously identified with clusterProfiler and associated with m^6A related genes were selected and their relationships were analyzed using ClueGO, enabling the visualization of shared genes between common terms. Calculation of network connectivity and comparison to random networks were performed using the igraph R package (https://cran.r-project.org/package=igraph). Differential exon usage analysis was performed with the DEXSeq R/Bioconductor package (Anders et al. 2012) on TPM normalized sequence counts quantified with Salmon v1.4.0 (Patro et al. 2017) in mapping-based mode using the stranded reverse library type parameter (-l SR).

Reference:

Anders S, Reyes A, Huber W. 2012. Detecting differential usage of exons from RNA-seq data. *Genome Res* **22**: 2008–17.

Bindea G, Galon J, Mlecnik B. 2013. CluePedia Cytoscape plugin: pathway insights using integrated experimental and in silico data. *Bioinformatics* **29**: 661–3.

Chen EY, Tan CM, Kou Y, Duan Q, Wang Z, Meirelles GV, Clark NR, Ma'ayan A. 2013. Enrichr: interactive and collaborative HTML5 gene list enrichment analysis tool. *BMC Bioinformatics* **14**: 128.

Doncheva NT, Morris JH, Gorodkin J, Jensen LJ. 2019. Cytoscape StringApp: Network Analysis and Visualization of Proteomics Data. *J Proteome Res* **18**: 623–632.

Lee S, Cook D, Lawrence M. 2019. plyranges: a grammar of genomic data transformation. *Genome Biol* **20**: 4.

Liao Y, Smyth GK, Shi W. 2019. The R package Rsubread is easier, faster, cheaper and better for alignment and quantification of RNA sequencing reads. *Nucleic Acids Res* **47**: e47.

Liu J, Dou X, Chen C, Chen Chuan and Liu C, Xu MM, Zhao S, Shen Bin and Gao Y, Han D, He C. 2020a. N 6-methyladenosine of chromosome-associated regulatory RNA regulates chromatin state and transcription. *Science (1979)* **367**: 580–586.

Liu J, Li K, Cai J, Zhang M, Zhang X, Xiong X, Meng H, Xu Xizhan and Huang Z, Peng J, Fan J, et al. 2020b. Landscape and Regulation of m6A and m6Am Methylome across Human and Mouse Tissues. *Mol Cell* **77**: 426–440.e6.

Liu J, Xu Y-P, Li K, Ye Q, Zhou H-Y, Sun H, Li X, Yu L, Deng Y-Q, Li R-T, et al. 2021. The m6A methylome of SARS-CoV-2 in host cells. *Cell Res* **31**: 404–414.

Love MI, Huber W, Anders S. 2014. Moderated estimation of fold change and dispersion for RNA-seq data with DESeq2. *Genome Biol* **15**: 550. http://www. (Accessed December 28, 2022).

Patro R, Duggal G, Love MI, Irizarry RA, Kingsford C. 2017. Salmon provides fast and bias-aware quantification of transcript expression. *Nat Methods* **14**: 417–419.

Riva L, Yuan S, Yin X, Martin-Sancho L, Matsunaga N, Pache L, Burgstaller-Muehlbacher S, de Jesus PD, Teriete P, Hull M v, et al. 2020. Discovery of SARS-CoV-2 antiviral drugs through large-scale compound repurposing. *Nature* **586**: 113–119.

Robinot R, Hubert M, de Melo Guilherme Dias and Lazarini F, Bruel T, Smith N, Levallois S, Larrous F, Fernandes J, Gellenoncourt S, Rigaud S, et al. 2021. SARS-CoV-2 infection induces the dedifferentiation of multiciliated cells and impairs mucociliary clearance. *Nat Commun* **12**: 4354.

Samelson AJ, Tran QD, Robinot R, Carrau L, Rezelj V v, Kain A mac, Chen M, Ramadoss GN, Guo X, Lim SA, et al. 2022. BRD2 inhibition blocks SARS-CoV-2 infection by reducing transcription of the host cell receptor ACE2. *Nat Cell Biol* **24**: 24–34.

Schmidt N, Lareau CA, Keshishian H, Ganskih S, Schneider C, Hennig T, Melanson R, Werner S, Wei Y, Zimmer M, et al. 2021. The SARS-CoV-2 RNA-protein interactome in infected human cells. *Nat Microbiol* **6**: 339–353.

Sun H, Li K, Zhang X, Liu J, Zhang M, Meng H, Yi C. 2021. m6Am-seq reveals the dynamic m6Am methylation in the human transcriptome. *Nat Commun* **12**: 4778.

Tan B, Liu H, Zhang S, da Silva SR, Zhang L, Meng J, Cui X, Yuan H, Sorel O, Zhang S-W, et al. 2018. Viral and cellular N6-methyladenosine and N6,2'-O-dimethyladenosine epitranscriptomes in the KSHV life cycle. *Nat Microbiol* **3**: 108–120.

Yu G, Wang L-G, Han Y, He Q-Y. 2012. clusterProfiler: an R package for comparing biological themes among gene clusters. *OMICS* **16**: 284–7.